# Analysis of spatiotemporal inner-outer large-scale interactions in turbulent channel flow by multivariate empirical mode decomposition

Esther Mäteling* and Wolfgang Schröder
RWTH Aachen University, Chair of Fluid Mechanics and Institute of Aerodynamics, 52062 Aachen, Germany

(Received 20 October 2021; accepted 25 February 2022; published 15 March 2022)

Research in the last decades has shown a strong interaction between near-wall turbulence and outer-layer large-scale motions in turbulent wall-bounded flows. In this paper, we propose a spatiotemporal multivariate approach based on state-of-the art methods of signal processing and a significantly enlarged data base to provide insight into the inner-outer interaction via superposition, bursts, and amplitude modulation. Spatially resolved, two-dimensional velocity fields within the viscous sublayer and the log layer are used to study spatial interactions. The temporal information provides insight into the temporal evolution of these features. In contrast to traditional studies, a noise-assisted multivariate empirical mode decomposition is applied to determine the involved scales. In this method, all velocity components of one time instant are simultaneously decomposed, which preserves intercomponent relations in the modal representations. In addition, the noise assistance ensures a temporal coherence of the resulting modes. Intermode comparisons, and thus the inner-outer interaction analysis, significantly benefit from this mode alignment by more precise findings, which is verified by comparisons with the univariate empirical mode decomposition results. The analysis reveals a considerable time-dependent behavior of the interaction phenomena with respect to the inner-outer correlation and the associated inclination angle. Regarding the superposition and the sweeps, the temporal variations are strongly linked to the rates of high-speed large scales to total large-scale fluctuations. The comparison to findings from purely temporal signals demonstrates distinct differences.

DOI: 10.1103/PhysRevFluids.7.034603

## I. INTRODUCTION

Research in the last decades has shown that near-wall turbulence and large-scale motions located inside the logarithmic layer strongly interact. Four phenomena—superposition, bursting events, amplitude modulation, and frequency modulation—are part of this inner-outer interaction. The superposition refers to the imprint of outer-layer streamwise-aligned large-scale structures on the near-wall flow field. The shift between these structures and their near-wall footprint is usually indicated by the inclination angle $\Theta_S$, which varies in the range $3^\circ \leqslant \Theta_S \leqslant 35^\circ$ [1].

The importance of bursting events, i.e., large-scale sweeps and ejections, in the inner-outer interaction was first addressed by Agostini and Leschziner [2] who noticed that positive large-scale perturbations cause considerably stronger modulation of the small scales than negative perturbations. To investigate the amplitude modulation of the near-wall flow field, which describes the changing strength of the near-wall fluctuations together with the outer-layer fluctuation level, several approaches have been presented, e.g., Refs. [3–5]. Recently, Mäteling *et al.* [6] introduced a technique in which the influence of the superposition is removed from the near-wall flow field prior to investigating the amplitude modulation. By determining the large-scale amplitudes directly

*Corresponding author: e.maeteling@aia.rwth-aachen.de

 

from the remaining near-wall and the outer-layer large scales via the Hilbert Transform, they clearly showed the high degree of inner-outer amplitude coherence.

A phenomenon less investigated is the frequency modulation of the small scales [7,8]. The associated phase lag between inner and outer fluctuations is comparable to that of the amplitude modulation in the near-wall region but with smaller magnitude [5]. Recent reviews concerning the phenomena of inner-outer interactions are given by Jiménez [9] and Marusic *et al.* [10].

Most experimental studies in this research field are based on hot-wire anemometry (HWA) data, i.e., temporal data of single-point measurements are used. To investigate spatial flow features, the application of Taylor's hypothesis of frozen turbulence [11] is required. The method became such an integral part in this field of research that it is hardly mentioned that the hypothesis is only valid under certain constraints, which are usually not met in the applied flow conditions. The key question is to which extent the spatial velocity field can be reconstructed based on a single mean convection velocity and temporally resolved data. In a comparative analysis in a turbulent boundary layer (TBL) flow by Dennis and Nickels [12] the velocity field obtained from spatially resolved particle-image velocimetry (PIV) measurements and that constructed from HWA measurements by applying Taylor's hypothesis were used to validate the latter approach. Besides qualitative similarity, the quantitative comparison showed significant differences increasing approximately linearly with projection distance. The authors mainly attributed this deviation to small-scale activities that are not maintained in time. Since the highest correlation coefficient between spatial and spatially reconstructed velocity field measures about 0.65, the approach should definitely be applied with caution. It was also shown by Atkinson *et al.* [13] that the extent over which Taylor's hypothesis can be applied increases with wall-normal distance when the local mean velocity is inserted as convection velocity.

To investigate how the spatial reconstruction of solely time-dependent data influences the conclusions drawn from the analysis of the inner-outer interaction, we use two-dimensional (2D) time-dependent flow fields and compare the results to conventionally used single-point time series. These pointwise signals are referred to as "0D" data since they do not possess direct spatial information. We use direct numerical simulation (DNS) data of a turbulent channel flow (TCF) at a friction Reynolds number based on the channel half-height $h$ of $\mathrm{Re}_\tau \approx 1000$ [14]. For the interaction analysis, we extend the recent approach by Mäteling *et al.* [6] from 0D temporal signals to 2D spatial data. The approach considers interactions by superposition, bursts, and amplitude modulation using the streamwise and the wall-normal velocity fluctuations in the viscous sublayer and at the log-layer location where the large scales are most energetic. The usage of spatially and temporally resolved data in the present study allows a much more thorough and more precise analysis of the structural interactions than pure 0D temporal signals since

(i) the spatial extent of the data captures spanwise movements and the meandering nature of the large scales can be considered,

(ii) the separate investigation of superposition and bursts provides detailed insight into the mechanisms of footprinting,

(iii) due to spatial correlations the temporal evolution of the large-scale interactions can be analyzed,

(iv) Taylor's hypothesis is not applied, its influence on the results can be studied.

The empirical mode decomposition (EMD) is used to determine the involved scales. The method was introduced by Huang *et al.* [15] for time-dependent, nonlinear signals and provides modal representations, called Intrinsic Mode Functions (IMFs), of the input data. Agostini and Leschziner [2] applied an extended 2D (spatial) version to DNS data of a TCF at $\mathrm{Re}_\tau = 1025$ to study inner-outer interactions. In the first application to experimental 2D data by Mäteling *et al.* [16] the superposition effect was studied. Note that in these investigations the 2D, wall-parallel flow data are decomposed separately with respect to the involved velocity components and the different wall-normal locations, which causes two essential disadvantages. First, an unequal number of decomposition levels is usually obtained, i.e., a varying number of IMFs for each velocity component and at different wall-normal positions. Second, the well-known phenomenon of mode mixing occurs, which is a consequence of signal intermittency causing an overlapping of the IMF spectra. Both phenomena usually prevent mode alignment, which means that the IMF at one wall-normal location contains different scales compared to the same-indexed mode at another wall-normal location and similarly for different velocity components. It goes without saying that these properties complicate the comparison of individual modes and thus, the investigation of mode-specific features like the interaction of large-scale motions.

Therefore, the current study introduces a multivariate version of the EMD algorithm (MEMD), which enables a simultaneous decomposition of all velocity components of interest at both wall-normal locations and preserves intercomponent relations within the modal representations. This mode alignment ensures that scales which are common to two or more velocity components are found in equal-indexed IMFs, which allows precise intermode comparisons. The algorithm is an extension of the 1D algorithm introduced by Rehman and Mandic [17] similarly to the bidimensional MEMD recently presented by Xia *et al.* [18] for image fusion applications. Note that the notation "multivariate" refers to multiple variables expressing flow properties, e.g., velocity components, pressure, and temperature, at distinct locations in the flow field, while "0D/2D" only defines the spatial dimensionality of the data.

Since the decomposition is performed in the spatial domain and thus, individually for each time step, a temporal coherence of the IMFs is not necessarily given. For a detailed analysis across the temporal domain, we use a noise-assisted MEMD (NA-MEMD) approach. Although the decomposition is data-driven, its "route" can be influenced via the input data and the noise assistance ensures similar properties of the IMFs of different time steps. Another useful characteristic is its reduced tendency to mode mixing, i.e., a smaller overlap of the IMF spectra, which provides a sharper scale separation.

The main objective of the manuscript is the introduction of a data-driven decomposition method, i.e., the two-dimensional noise-assisted multivariate empirical mode decomposition, to the field of fluid dynamics and the demonstration of its successful application for a well-known problem, the interaction between outer-layer large-scale structures and the near-wall flow field in turbulent wall-bounded flows. It is shown that the 2D NA-MEMD extracts temporally coherent 2D flow structures, which are categorized into modes with increasing scale size, and outperforms the standard 2D EMD due to its exceptional mode alignment across different velocity fluctuation components and wall-normal distances in the spatial and temporal domain. This property enhances the subsequent inner-outer interaction analysis and provides further insight into the time-dependent flow phenomena.

The manuscript is structured as follows. First, an overview of the used DNS data is given in Sec. II. Section III covers a description of the 2D NA-MEMD algorithm for scale separation (Sec. III A) and outlines the procedure to study the inner-outer interactions of the large scales with respect to superposition, bursting events, and amplitude modulation (Sec. III B). The results are presented in Sec. IV, which is divided into four parts. First, the IMF properties are briefly discussed. Subsequently, the results of the spatial interaction analysis are given for an exemplary time step (Sec. IV B). This is followed in Sec. IV C by the study of the temporal evolution of the spatial interactions. Then, the time-averaged results are compared to the findings of the 0D analysis in Sec. IV D. Finally, conclusions are drawn in Sec. V. In addition to Sec. III A, Appendix A provides detailed insight into the NA-MEMD algorithm. It covers supplementary material for in-depth understanding of the working principle (Appendices A 1 and A 2), a discussion of application-related parameter choices (Appendix A 3), and a comparison between the univariate EMD, the MEMD, and the NA-MEMD (Appendix A 4) proving the superior performance of the NA-MEMD for scale separation in the context of this study. The latter is supported by Appendix B, which provides results of the inner-outer interaction analysis based on a univariate EMD for scale separation. In Appendix C it is shown how to calculate 2D amplitude distributions based on the 2D analytic signal, which are used for studying the amplitude modulation.

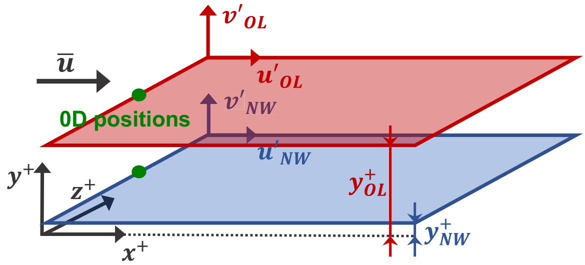


FIG. 1. Schematic arrangement and notation of the data used for the inner-outer interaction analysis.

## II. NUMERICAL DATA

The DNS data of a TCF at $\mathrm{Re}_\tau \approx 1000$ from the *Johns Hopkins Turbulence Database* [14,19,20] is used. The domain size of the simulation measures $L_x \times L_y \times L_z = 8\pi h \times 2h \times 3\pi h$, where $x$ denotes the streamwise, $y$ the wall-normal, and $z$ the spanwise direction. The channel half-height equals $h = 1$ in dimensionless units. The simulation comprises $2048 \times 512 \times 1536$ nodes on a grid with cell sizes of $\Delta x^+ = 12.2639$, $\Delta z^+ = 6.13196$, and varying spacing in the wall-normal direction with $\Delta y^+ = 1.65199 \times 10^{-2}$ at the wall and $\Delta y^+ = 6.15507$ at the centerline. The superscript + denotes quantities in inner units, i.e., a nondimensionalization with the friction velocity $u_\tau$ and the kinematic viscosity $\nu$. In total, 4000 time steps are available, which are highly resolved with a spacing of $\Delta t^+ = 0.325$ that results in a total length of $t^+ \approx 1300$. Note that the DNS possesses a time step of $\Delta t^+ = 0.065$ but only every fifth snapshot is stored. For more information about the DNS data set, the reader is referred to Graham *et al.* [14].

For the current investigation, 2D wall-parallel slices of the streamwise $u'$ and the wall-normal $v'$ velocity fluctuations are extracted with a domain size of $x^+ \times z^+ \approx 6140 \times 3070$. The flow data are taken at two wall-normal distances $y^+_{\mathrm{NW1}} = 1$ and $y^+_{\mathrm{NW5}} = 5$ for the inner location, denoted by the subscripts NW1 and NW5 (near wall), and at $y^+_{\mathrm{OL}} = 123$ for the outer location, denoted by the subscript OL (outer layer). The latter is the position where the large-scale motions are most energetic, which is defined by $y^+_{\mathrm{OL}} = 3.9\sqrt{\mathrm{Re}_\tau} = 123$ [21]. A sketch of the arrangement of the extracted data is given in Fig. 1. In the temporal domain, every tenth time step is used, i.e., the spacing between consecutive data points measures $\Delta t^+ = 3.25$.

The 2D results are compared to the usually used 0D time-dependent signals in Sec. IV D. Therefore, another data set of streamwise and wall-normal velocity fluctuations is extracted at a fixed streamwise and spanwise position within the domain of the 2D data and with the same wall-normal locations (denoted “0D positions” in Fig. 1). While every tenth time step is used in the 2D data, all available time steps are considered to obtain a temporal resolution comparable to HWA data.

## III. METHODOLOGY

The analyses of inner-outer interactions are based on the assumption that common features exist in different layers of wall-bounded flows. However, conventional approaches perform a scale separation individually for each quantity and compare the resulting scales subsequently. Why aren’t possible intercomponent relations considered directly during the scale separation process? This is exactly what is possible by a multivariate EMD approach. Therefore, we introduce the 2D noise-assisted multivariate EMD (NA-MEMD) algorithm to this field of research. The question arises whether or not this is necessary since previous studies by, e.g., Agostini and Leschziner [2] and Mäteling *et al.* [16], obtained meaningful results using the less complex 2D univariate EMD approach. However, these results required a careful handling of the modal representations by experienced researchers. This subjectivity can be strongly eliminated by applying an NA-MEMD.

In addition, the former findings can be easily refined using the NA-MEMD due to its automated consideration of data-inherent relations directly within the scale separation and the exceptional temporal coherence between subsequent IMFs. Appendix A 4 provides valuable comparisons between the modes resulting from a univariate EMD, an MEMD, and an NA-MEMD to emphasize the aforementioned benefits. In addition, results of the inner-outer interaction analysis based on a scale separation by a univariate EMD are given in Appendix B, which show the superior performance of the NA-MEMD for the current application.

In the following, a short general introduction to the EMD algorithms is given in Sec. III A before the 2D NA-MEMD algorithm is outlined. The 2D procedure of the inner-outer interaction analysis is described in Sec. III B.

### A. Two-dimensional noise-assisted multivariate empirical mode decomposition

The EMD was originally proposed by Huang *et al.* [15] to physically meaningfully process nonlinear and unsteady temporal data. The decomposition works empirically since the data itself dictates the decomposition. The resulting IMFs are solely based on the characteristic timescales inherent to the data. Thus, the modes are adaptively biased towards locally dominant frequencies, which enables the extraction of physically relevant unsteady processes in a finite bandwidth.

An extension of the single-dimension EMD to a 2D method, also known as bidimensional EMD, was first presented by Nunes *et al.* [22] for a texture analysis algorithm. It was applied to 2D fluid flow data in the context of scale separation by, e.g., Agostini and Leschziner [2] and Mäteling *et al.* [16]. The 2D, wall-parallel flow data are decomposed separately at different wall-normal locations, which prevents a precise scale alignment in corresponding IMFs and complicates or even falsifies the subsequent inner-outer interaction analysis.

To tackle the problems of uniqueness, mode mixing, and mode alignment, a multivariate EMD (MEMD) approach for time-dependent data was introduced by Rehman and Mandic [17]. The essential step in performing the EMD is the calculation of a local mean, which strongly depends on the determination of local maxima and minima. For multivariate signals, however, it is not straightforward to detect these extrema, since the fields of complex and hypercomplex numbers are not ordered. This challenge was overcome by using real-valued signal projections along multiple directions on hyperspheres [17]. The approach was recently extended to two dimensions by Xia *et al.* [18] in the context of image fusion applications. Since the main objective of extracting common spatiotemporal scales across multiple images is comparable to the present fluid dynamical application, this approach is the basis for our scale separation algorithm.

In addition, we incorporate the concept of "noise-assistance," which was introduced for the single-dimension MEMD by Rehman and Mandic [23] and Rehman *et al.* [24] and builds on studies of Wu and Huang [25] and Flandrin *et al.* [26]. It was shown in the latter studies that the classical EMD essentially behaves as a dyadic filter when decomposing white and Gaussian noise. Thus, the resulting modes are normally distributed and possess identical Fourier spectra with doubled mean periods of neighboring IMFs [25]. The filter bank property was used in Refs. [23,24] to improve frequency localization and to reduce mode mixing by decomposing the multivariate data with additional variates of pure Gaussian noise. Once the decomposition is finished, the IMFs related to the noise data are disregarded since they were only necessary to impose the desired properties. In the current application, the noise assistance, i.e., the 2D NA-MEMD, enhances the temporal continuity of the IMFs compared to the 2D MEMD algorithm. The interested reader is referred to Appendix A 4 for a detailed comparison of both methods.

In the following, a high-level overview of the applied 2D NA-MEMD is given. Figure 2 summarizes the algorithm and Table I provides an overview of the used notation. The presentation of the NA-MEMD algorithm assumes a fundamental knowledge about existing EMD algorithms. The reader is referred to Ref. [17] for a general description with respect to time-dependent multivariate signals and to Ref. [6] for a thorough introduction of the 1D EMD method for scale separation

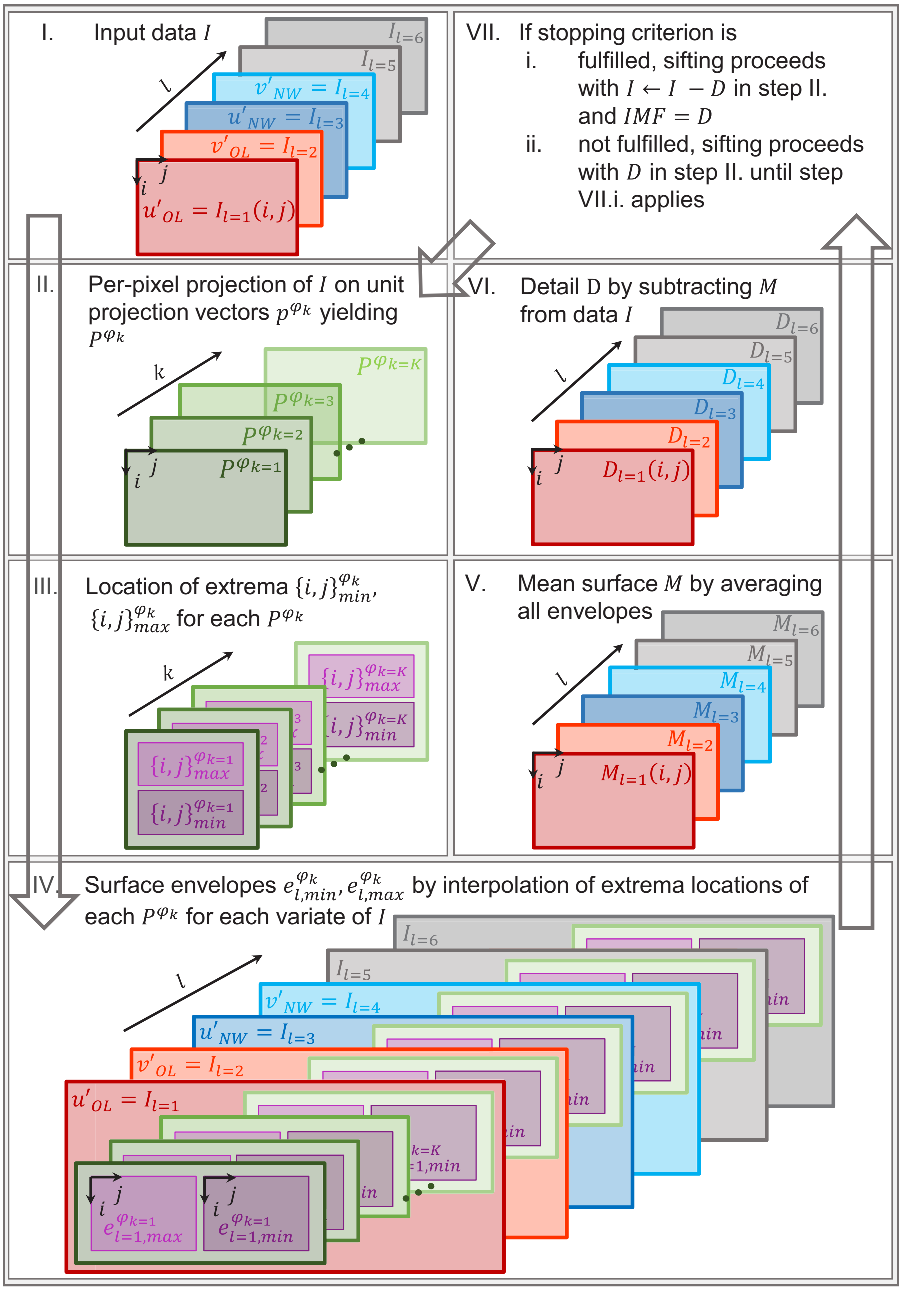


FIG. 2. 2D NA-MEMD algorithm.

in turbulent fluid flows. Appendix A offers further insight into the 2D NA-MEMD algorithm and respective references are given throughout this section.

The 2D NA-MEMD method projects a 2D multivariate signal on a unit hypersphere in a multidimensional space via real-valued surface projections and estimates the mean surface by interpolation and averaging. In the current application, the 2D multivariate signal consists of six "channels" ($L = 6$). Four of these channels ($l = 1 - 4$) are 2D wall-parallel snapshots of the fluid flow at

TABLE I. Notation used in the presentation of the 2D NA-MEMD algorithm.

| | |
|---|---|
| $D$ | Detail |
| $e$ | Surface envelope |
| $i$ | First dimension of $I$ |
| $I$ | Input array |
| $j$ | Second dimension of $I$ |
| $k$ | Projection direction |
| $K$ | Total number of projection directions |
| $l$ | Channel, third dimension of $I$ |
| $L$ | Total number of channels |
| $M$ | Mean surface envelope |
| min | Minima |
| max | Maxima |
| $p$ | Projection vector |
| $P$ | Projected signal |
| $\varphi_k$ | Projection angle |

a single time step using the streamwise and the wall-normal velocity fluctuations at a near-wall and an outer-layer location ($u'_{\mathrm{NW}}, v'_{\mathrm{NW}}, u'_{\mathrm{OL}}, v'_{\mathrm{OL}}$). The two remaining channels ($l = 5, 6$) consist of random Gaussian noise with zero mean and spatial dimensions identical to the flow data. The noise power is set to 2% of the variance of the flow data and hence, the noise channels are renewed for each time step. The choice for the number of noise channels and the noise power are discussed in Appendix A 3 a.

All six 2D arrays are stacked together resulting in a 3D array $I$ in which the third dimension $l$ incorporates the six channels. In the first step of the sifting process, the multivariate values of each location defined by the pixel $(i, j)$ are considered separately. They are projected onto several unit projection vectors $p^{\varphi_k}$ where $k$ denotes the projection direction. The choice of the total number of projection directions $K = 22$ is discussed in Appendix A 3 b. The angles $\varphi_k$ are distributed along the $(L-1)$ sphere as obtained from a low-discrepancy Hammersley sequence [17,18]. The projection of $I$ on $p^{\varphi_k}$ is denoted by $P^{\varphi_k}$ and given for a single pixel $(i, j)$ by

$$P^{\varphi_k}(i, j) = \sum_{l=1}^{L} p_l^{\varphi_k} I_l(i, j). \tag{1}$$

Applying this projection to all pixels yields $K$ 2D univariate signals. Subsequently, the local extrema of each projection $P^{\varphi_k}$ are determined by a neighboring window method yielding $K$ sets of minima $\{i, j\}_{\mathrm{min}}^{\varphi_k}$ and maxima $\{i, j\}_{\mathrm{max}}^{\varphi_k}$ locations. An interpolation of the original data at these positions by Delaunay triangulation results in a set of one minima $e_{l,\mathrm{min}}^{\varphi_k}$ and one maxima $e_{l,\mathrm{max}}^{\varphi_k}$ surface envelope for each projection direction $k$ and each variate $l$ [18]. These sets are averaged over all projection directions

$$M_l = \frac{1}{2K} \sum_{k=1}^{K} \left(e_{l,\mathrm{min}}^{\varphi_k} + e_{l,\mathrm{max}}^{\varphi_k}\right) \tag{2}$$

to obtain a single mean surface $M_l$ for each variate, i.e., six surfaces for the current data set. The mean surface is subtracted from the original data yielding the detail $D = I - M$. If the stopping criterion, which is discussed thoroughly in Appendix A 2, is fulfilled, the detail $D$ is the first IMF and the described procedure is repeated for the remaining data $I - D$. Otherwise, the detail $D$ is further decomposed by the described process, i.e., another sifting is employed, until the stopping criterion is reached. In Appendix A 1, step-by-step visualizations of one sifting process of velocity data are provided for a more in-depth understanding. The modes of the noise channels are neglected after the decomposition since they were only relevant to impose the filter bank property.

To process the 0D data, i.e., the solely time-dependent signals, the MEMD algorithm published by Rehman and Mandic [17] is used. As for the 2D data, two noise channels with a variance of 2% of the velocities' variance are appended to the data prior to the decomposition.

After successful decomposition, modal representations have to be allocated to the large scales for the inner-outer interaction analysis. In this study, small- and medium-size scales extracted from the 2D data are described by the first four IMFs and the sum of the remaining modes represents the large scales. The resulting large scales within the log layer possess similar properties as described in former studies, e.g., a streamwise extent on the order of three channel half-heights [27] and a spanwise spacing of around 0.48 channel half-heights [28,29]. For the 0D data, all modes above the ninth IMF are summed to represent the large scales. Their properties are consistent with a recent study using the temporal MEMD for scale separation within a temporal 0D interaction analysis [30]. The application of Taylor's hypothesis yields streamwise length scales on the same order as the 2D large-scale structures. Note that the present data-driven decomposition involves an *a posteriori* definition of the large scales. This is in contrast to the a priori definition of the traditional spectral filtering using a preset cutoff value.

Finally, the computational cost associated with each EMD algorithm are briefly addressed. For the 0D data comprising time series with 4000 time steps of the four velocity variates ($u'_{\mathrm{OL}}$, $v'_{\mathrm{OL}}$, $u'_{\mathrm{NW}}$, $v'_{\mathrm{NW}}$) and two noise channels, the NA-MEMD is about two orders of magnitude slower compared to the four consecutive univariate EMDs. However, the computing time of the NA-MEMD is still less than 10 seconds on a standard computer with an *Intel i5 (4 cores 3.2 GHz)* processor. The difference between uni- and multivariate EMD performances increases for the 2D algorithms. The 2D NA-MEMD is about 40 times slower than the 2D univariate EMD and requires approximately 48 h on a high-performance computing cluster using 40 cores simultaneously to decompose all 400 time steps. Although the computational cost substantially increase with the multivariate approaches, the addressed ability of adequately capturing physical relations directly within the scale separation and thus, increasing the precision of the inner-outer interaction justifies the higher effort.

### B. Two-dimensional inner-outer interaction

The inner-outer interaction of large-scale motions is investigated by using wall-parallel, 2D snapshots of the streamwise and the wall-normal velocity fluctuations at an inner and an outer wall-normal location. For each instance in time, the 2D NA-MEMD is applied simultaneously to all four velocity components as described in Sec. III A to determine the inherent large scales, denoted by LS. Although each time step is treated separately, the excellent performance of the 2D NA-MEMD algorithm ensures a physically meaningful temporal evolution of the scales in each IMF. This is certainly only possible for a sufficient temporal resolution of the data. Time series of exemplary IMFs and large-scale flow fields are given in movies provided in the Supplemental Material [34,41].

The inner-outer interaction is studied for the phenomena of superposition, sweeps, ejections, and amplitude modulation. The applied procedure is a 2D multivariate extension of the 0D time-dependent approach described in Ref. [6], in which solely the streamwise velocity fluctuations are used. The extended approach additionally considers the wall-normal velocity fluctuations to allow a detailed investigation of the bursting events. Since its results are compared to the 0D findings to study how well time-dependent approaches can represent spatial interactions, the 0D wall-normal velocity component is also incorporated into the 0D analysis for a fair comparison.

In the following, the procedure to study the inner-outer interactions is outlined. The formulas are given with respect to the 2D data but essentially, the spatial coordinates can be replaced by the temporal coordinate to obtain the equations for the 0D analysis, which are discussed in detail in Refs. [6,30].

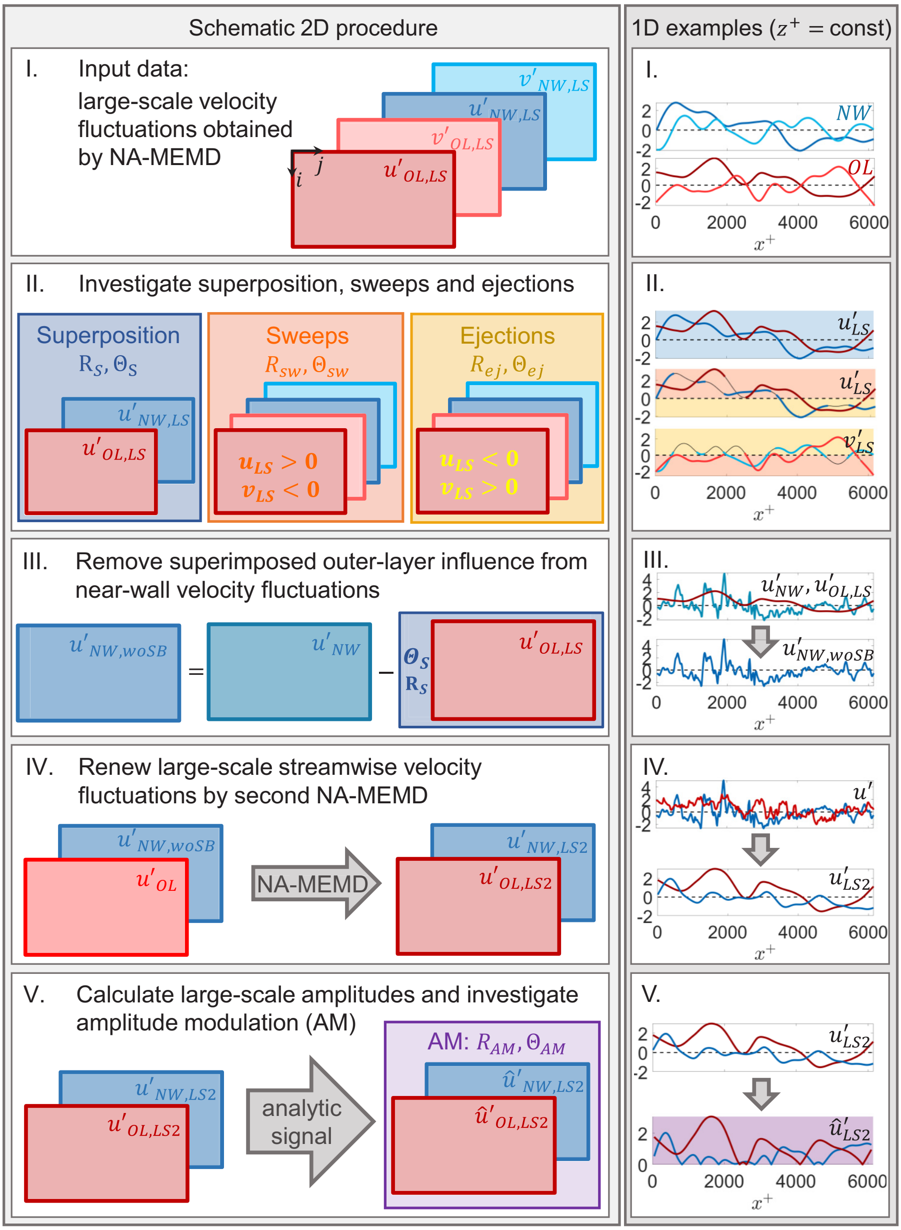


FIG. 3. Schematic procedure used to study the 2D large-scale inner-outer interactions. Exemplary 1D streamwise data at a fixed spanwise position ($z^+$ = const) are additionally provided.

A schematic overview about all steps involved in the interaction analysis is given in Fig. 3. To enhance the understanding, exemplary 1D streamwise signals at a fixed spanwise position are given for each step. Note that the data are normalized by the respective root-mean square (rms) values due to the magnitude differences of inner- and outer-layer quantities. Figure 3 shows that the scale decomposition by the NA-MEMD is followed by the investigation of the superposition and the bursts. The superposition—denoted by the subscript $S$—refers to the streamwise shift imposed

TABLE II. Definition of correlation coefficients and involved quantities related to Eqs. (3) and (4). The quantity $q'_{\mathrm{NW}}$ represents the near-wall large-scale and the quantity $q'_{\mathrm{OL}}$ the outer-layer large-scale velocity fluctuations involved in the considered phenomenon, i.e., $u'_{\mathrm{NW,LS}}$, $u'_{\mathrm{NW,LS}} + iv'_{\mathrm{NW,LS}}$, $\hat{u}'_{\mathrm{NW,LS2}}$ and $u'_{\mathrm{OL,LS}}$, $u'_{\mathrm{OL,LS}} + iv'_{\mathrm{OL,LS}}$, $\hat{u}'_{\mathrm{OL,LS2}}$, and the subscript $A$ denotes the respective abbreviation, i.e., superposition ($S$), sweeps (sw), ejections (ej), amplitude modulation (AM).

| $R_A$ | Superposition $R_S$ | Sweeps $R_{\mathrm{sw}}$ | Ejections $R_{\mathrm{ej}}$ | Amplitude modulation $R_{\mathrm{AM}}$ |
|---|---|---|---|---|
| $q'_{\mathrm{NW}}$ | $u'_{\mathrm{NW,LS}}$ | $u'_{\mathrm{NW,LS,sw}} + iv'_{\mathrm{NW,LS,sw}}$ | $u'_{\mathrm{NW,LS,ej}} + iv'_{\mathrm{NW,LS,ej}}$ | $\hat{u}'_{\mathrm{NW,LS2}}$ |
| $q'_{\mathrm{OL}}$ | $u'_{\mathrm{OL,LS}}$ | $u'_{\mathrm{OL,LS,sw}} + iv'_{\mathrm{OL,LS,sw}}$ | $u'_{\mathrm{OL,LS,ej}} + iv'_{\mathrm{OL,LS,ej}}$ | $\hat{u}'_{\mathrm{OL,LS2}}$ |

by the outer-layer large scales onto the near-wall flow field. Thus, only the large-scale streamwise velocity fluctuations $u'_{\mathrm{NW,LS}}$, $u'_{\mathrm{OL,LS}}$ are needed to analyze this phenomenon.

To investigate the bursting events of sweeps and ejections, the wall-normal large-scale components are considered as well. Via quadrant analysis, large-scale sweeps—denoted by the subscript sw—can be identified at locations where $\{u'_{\mathrm{LS}} > 0, v'_{\mathrm{LS}} < 0\}$, while ejections—denoted by the subscript ej—occur for the conditions $\{u'_{\mathrm{LS}} < 0, v'_{\mathrm{LS}} > 0\}$. Thus, $u'_{\mathrm{LS,sw}}$ solely contains positive streamwise fluctuations with the constraint that the respective wall-normal component $v'_{\mathrm{LS,sw}}$ is negative. Otherwise, the quantities are zero and the same holds for $u'_{\mathrm{LS,ej}}$, $v'_{\mathrm{LS,ej}}$ with reversed signs. The analysis of near-wall and outer-layer bursts reveals to which extent sweeps of the outer layer reach the near-wall area and vice versa for the ejections. Thus, it provides deeper insight into the mechanisms of the superposition. Note that our analysis showed that the $Q1$ events with $\{u'_{\mathrm{LS}} > 0, v'_{\mathrm{LS}} > 0\}$ and the $Q3$ events with $\{u'_{\mathrm{LS}} < 0, v'_{\mathrm{LS}} < 0\}$ hardly provide any contribution to the inner-outer interaction and are not shown for brevity.

To study the inner-outer interaction of all phenomena, the near-wall and the outer-layer quantities are correlated by

$$R_A(\Delta x^+, \Delta z^+) = \frac{\sum_{x^+}\sum_{z^+}[q'_{\mathrm{NW}}(x^+, z^+)q'^{\star}_{\mathrm{OL}}(x^+ + \Delta x^+, z^+ + \Delta z^+)]}{\sqrt{\sum_{x^+}\sum_{z^+}|q'_{\mathrm{NW}}(x^+, z^+)|^2}\sqrt{\sum_{x^+}\sum_{z^+}|q'_{\mathrm{OL}}(x^+ + \Delta x^+, z^+ + \Delta z^+)|^2}}. \tag{3}$$

The star symbol denotes complex conjugation, the vertical lines indicate absolute values, and the quantities $R_A$, $q'_{\mathrm{NW}}$, $q'_{\mathrm{OL}}$ for each event are given in Table II. Thus, the quantity $q'$ represents the particular velocity fluctuations involved in the considered phenomenon and the subscript $A$ is the respective abbreviation. That is, $q'$ is $u'_{\mathrm{LS}}$ or $u'_{\mathrm{LS}} + iv'_{\mathrm{LS}}$ and $R_A$ is $R_S$, $R_{\mathrm{sw}}$, or $R_{\mathrm{ej}}$. To consider both conditions for the bursts, the streamwise and the wall-normal components are combined to a complex velocity distribution $u'_{\mathrm{LS}} + iv'_{\mathrm{LS}}$ prior to correlation. Note that for completeness the quantities for the amplitude modulation denoted by the subscript AM, i.e., the amplitudes $\hat{u}'_{\mathrm{LS2}}$ and the correlation coefficient $R_{\mathrm{AM}}$, are also listed in the table.

As indicated in Eq. (3), the outer-layer component $q'_{\mathrm{OL}}$ is shifted pixelwise by $\Delta x^+$ in the streamwise and by $\Delta z^+$ in the spanwise direction, i.e., with increments of 12.26 and 6.13 viscous units, such that a 2D correlation map $R_A$ is generated. For meaningful correlations, the shift is restricted to values smaller than half of the entire spatial domain. The spatial shift $(\Delta x^+_A, \Delta z^+_A)$ associated with the maximum correlation coefficient $R_{A,\max}$ is used to calculate the inclination angle

$$\Theta_A = \mathrm{sgn}(\Delta x^+_A)\tan^{-1}\left(\frac{y^+_{\mathrm{OL}} - y^+_{\mathrm{NW}}}{\sqrt{(\Delta x^+_A)^2 + (\Delta z^+_A)^2}}\right), \tag{4}$$

where the index $A$ is to be replaced according to Table II and the expression $\mathrm{sgn}(\Delta x^+_A)$ refers to the sign of $\Delta x^+_A$. A positive angle indicates leading outer-layer structures. Due to the two-dimensionality of the data, the meandering nature of the large-scale fluctuations can be considered by spanwise shifts in the correlation coefficient as well as in the inclination angle. First investigations on this meandering behavior have been performed for the superposition phenomenon by Mäteling *et al.* [16] showing a small reduction in the inclination angle when the spanwise component was incorporated.

In a subsequent step, the superimposed outer-layer influence is removed from the total near-wall streamwise fluctuations $u'_{\mathrm{NW}}$ via Eq. (5). Essentially, a shifted and scaled version of the streamwise outer-layer large-scale signal $u'_{\mathrm{OL,LS}}$ is subtracted from $u'_{\mathrm{NW}}$. The signal $u'_{\mathrm{OL,LS}}$ is shifted with respect to the inclination angle $\Theta_S$ such that features related between both wall-normal layers are subsequently determined at the same $(x^+, z^+)$ locations. Furthermore, the shifted signal is scaled by the maximum correlation coefficient $R_{S,\max}$. Since this quantity is a measure of similarity between the large scales at both wall-normal positions and thus, represents the impact of the outer layer on the near-wall flow, i.e., the strength of interaction, it determines the amount of outer-layer influence that needs to be removed from the near-wall signal. The additional multiplication by the ratio $\mathrm{rms}(u'_{\mathrm{NW,LS}})/\mathrm{rms}(u'_{\mathrm{OL,LS}})$ compensates for magnitude differences between the large scales of both layers. Although Eq. (5) technically only uses quantities related to the superposition, i.e., $\Theta_S$ and $R_{S,\max}$, the impact of sweeps and ejections is indirectly included by its effect on the streamwise large scales. The separate investigation of the bursting events solely serves the purpose of inspecting the specific dynamics of the superposition phenomenon in more detail.

$$u'_{\mathrm{NW,woSB}}(x^+, z^+) = u'_{\mathrm{NW}}(x^+, z^+) - R_{S,\max} u'_{\mathrm{OL,LS}}(x^+, z^+, \Theta_S) \frac{\mathrm{rms}(u'_{\mathrm{NW,LS}})}{\mathrm{rms}(u'_{\mathrm{OL,LS}})}. \tag{5}$$

The motivation for calculating a near-wall signal with fewer outer-layer influences, i.e., only amplitude and frequency modulation remain, is twofold. On the one hand, it is the first step of the challenging process to obtain a statistically universal near-wall signal, which would allow the prediction of the fluctuating velocity statistics in the near-wall region given only the outer-layer data as proposed by Marusic *et al.* [31]. On the other hand, and this is very essential for the current analysis, it was shown in Mäteling *et al.* [6] for 0D data that once the influence of the superimposed outer-layer large scales is eliminated from the near-wall signal, the study of amplitude modulation more clearly reveals the remaining outer-layer impact. Therefore, a second scale decomposition of the remaining near-wall signal was conducted to obtain updated near-wall large-scale components, which obviously possess smaller wavelengths compared to the original large scales. This indicates that the amplitude modulation does not act on the largest near-wall scales but possesses slightly smaller variations within the large-scale amplitudes.

In the current study, a second 2D NA-MEMD of a four-channel signal consisting of $u'_{\mathrm{NW,woSB}}$, i.e., the outcome of Eq. (5), the total, unmodified outer-layer streamwise fluctuations $u'_{\mathrm{OL}}$, and two noise channels is performed. To save computational power, the wall-normal velocity component is excluded from the second NA-MEMD since it is irrelevant for the amplitude modulation analysis. From the resulting large-scale components $u'_{\mathrm{NW,LS2}}$, $u'_{\mathrm{OL,LS2}}$ of the second NA-MEMD, the large-scale amplitudes $\hat{u}'_{\mathrm{NW,LS2}}$, $\hat{u}'_{\mathrm{OL,LS2}}$ are determined. It was shown in Ref. [6] that this approach is superior in detecting the amplitude modulation compared to the typically used large-scale trend of the small-scale signal introduced by Mathis *et al.* [3]. The large-scale amplitudes are correlated based on Eq. (3) and the maximum correlation coefficient reflects the similarity of the near-wall and the outer-layer amplitudes, i.e., the strength of the amplitude modulation. Similar to the phenomena of superposition and bursting events, the position of this correlation peak is used to obtain the inclination angle by Eq. (4).

In the 0D approach, the amplitudes are defined as the amplitudes of an analytic signal, in which the real part is defined by the large-scale signal and the imaginary part by the Hilbert Transform of the former [6]. However, it is not straightforward to define a unique analytic signal in 2D. Wietzke *et al.* [32] introduced the 2D analytic signal, which is an extension of the monogenic signal [33] and enables the analysis of intrinsic 2D structures. To calculate 2D amplitudes based on this approach, the large-scale velocity field is embedded into 3D projective space such that geometric features (orientation, apex angle) and structural features (phase, amplitude) can be differentiated. All features

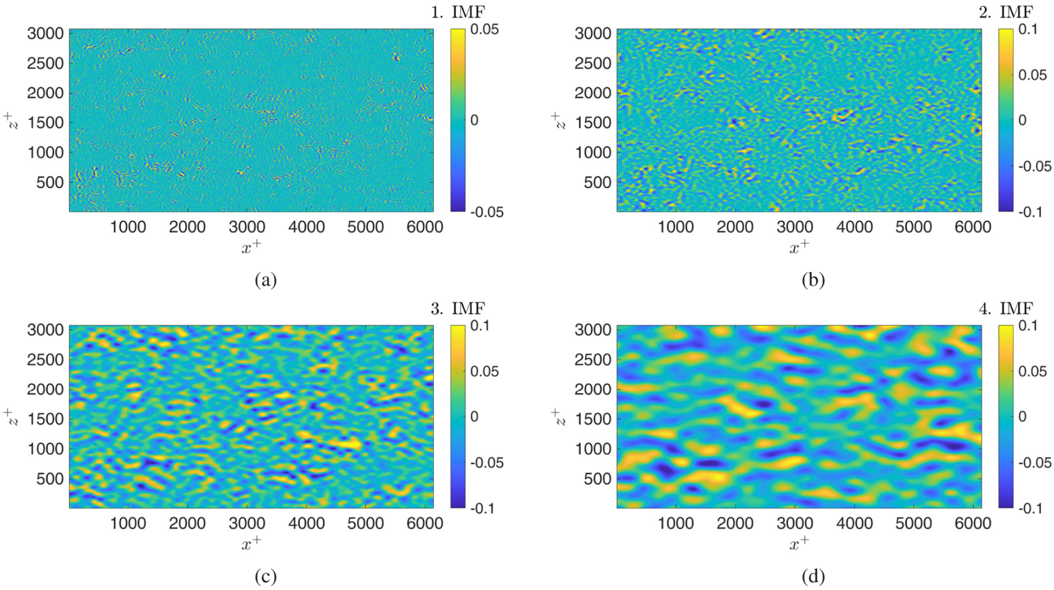


FIG. 4. (a) 1. IMF, (b) 2. IMF, (c) 3. IMF, and (d) 4. IMF of the streamwise outer-layer flow at $y^+_{\mathrm{OL}} = 123$ and $t^+ = 36$, which is simultaneously decomposed with the data at $y^+_{\mathrm{NW1}} = 1$.

are calculated localized using a $7\times7$ convolution mask. By using first- and second-order 2D Hilbert convolution kernels, first- and second-order Hilbert transformed velocity components are obtained, which finally yield the desired amplitudes. A detailed description how amplitudes are obtained from this approach is outlined in Appendix C.

Again, we emphasize that the complete analysis is conducted in the spatial domain individually for each time step. Thus, it is possible to study the temporal evolution of all phenomena and obtain in-depth information about temporal trends that could yet not be determined by the 0D-time-series analysis since the 0D approach provides only a single correlation peak and inclination angle for each phenomenon representing the averaged interaction across the whole time span.

## IV. RESULTS

This discussion is divided into four parts. First, properties of the IMFs resulting from the 2D NA-MEMD algorithm are discussed in Sec. IV A. Subsequently, instantaneous results of the 2D multivariate inner-outer interaction analysis for an exemplary time step are presented (Sec. IV B). The time-dependent features of the 2D inner-outer interactions are discussed in Sec. IV C. The time-averaged results of the 2D analysis are compared with the 0D results in Sec. IV D.

### A. Intrinsic mode functions

The streamwise and wall-normal velocity fluctuations at $\{y^+_{\mathrm{NW1}} = 1, y^+_{\mathrm{OL}} = 123\}$ of an arbitrarily chosen time step $t^+ = 36$ are decomposed by the 2D NA-MEMD. The resulting first four modes of the streamwise outer-layer data are given in Fig. 4. The IMFs with higher mode number represent large-scale structures and are discussed in detail in the following sections. It is obvious from Fig. 4 that the streamwise and spanwise wavelengths increase with increasing mode number. A movie that is provided in the Supplemental Material [34] shows the temporal evolution of these IMFs. Although the modes are separately determined for each time step, i.e., no temporal information is used during the decomposition, they are continuous in time. This behavior corroborates that the applied NA-MEMD algorithm extracts physically relevant scales and precisely differentiates them

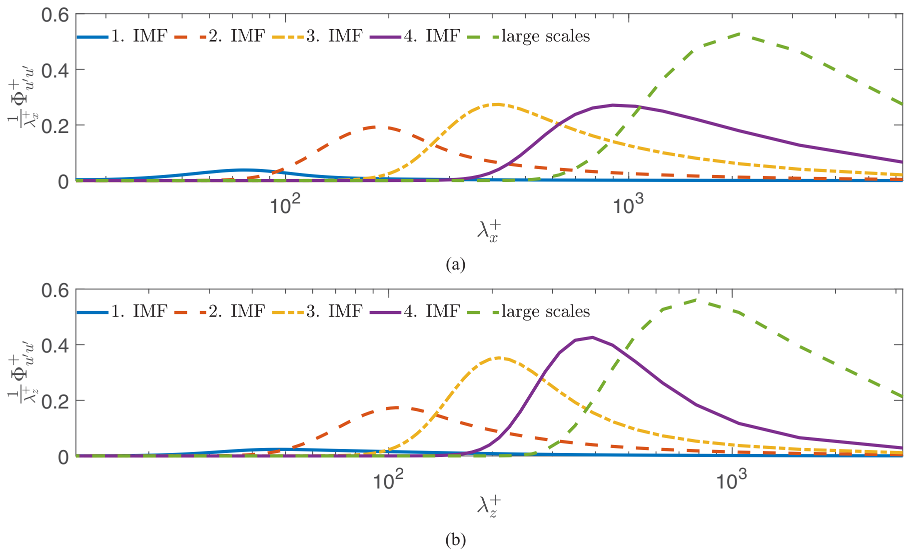


FIG. 5. Time-averaged premultiplied streamwise energy spectra $\frac{1}{\lambda^+}\Phi^+_{u'u'}$ of the outer-layer flow in the (a) streamwise and (b) spanwise direction.

into the respective modes. Of course, the IMFs of the other velocity components share this property. They are not visualized for conciseness.

To further assess the properties of the IMFs, time-averaged premultiplied streamwise energy spectra $\frac{1}{\lambda^+}\Phi^+_{u'u'}$ are calculated. Here and throughout this manuscript, temporal averages are determined by taking the arithmetic mean. The respective spectra of the outer-layer IMFs in the streamwise and spanwise direction are plotted in semi-logarithmic scale in Fig. 5. As observed in Fig. 4, the wavelengths increase with increasing mode number. The transition is smooth, i.e., although a specific range of scales can be attributed to each individual IMF, an overlapping area between neighboring modes exists. This has the advantage that related features can be assigned to the same mode although their scales deviate from the mode's prevailing scale size. It additionally allows the features within one IMF to grow or shrink in time within a certain range. This ensures that physically relevant growth processes are covered and that the respective features are not switching back and forth between neighboring modes. The assignment to different modes can rather be interpreted as a segmentation between physically connected structures than a distinct separation between wavelengths, which is usually obtained via spectral filtering by using rigorous cutoff values. The modes resulting from the latter approach potentially do not share any physical properties, which is undesired for the present purpose of data decomposition. Thus, a physical segmentation is ensured by the applied decomposition strategy, which is advantageous for the subsequent inner-outer interaction analysis.

Figure 5 shows that the center wavelengths between neighboring IMFs are approximately doubled. This is imposed by the dyadic filter bank property of the Gaussian noise concatenated with the velocity data for the decomposition. The range of streamwise wavelengths in each IMF encloses higher values compared to the spanwise wavelengths, which indicates that the scales of all IMFs possess a preferential orientation in the main flow direction. The energy content within each mode increases with the mode number, i.e., larger scales tend to carry more energy. This supports previous conclusions by, e.g., Liu *et al.* [27] and Balakumar and Adrian [35], stating that the largest scales in wall-bounded flows carry most of the energy. It is important to note that this energy distribution is not enforced by the NA-MEMD algorithm in contrast to, e.g., a proper orthogonal decomposition, which has also been used for scale separation in the past [27,36]. Hence, the different approach of the NA-MEMD method could be used to support conclusions about the energy distribution between

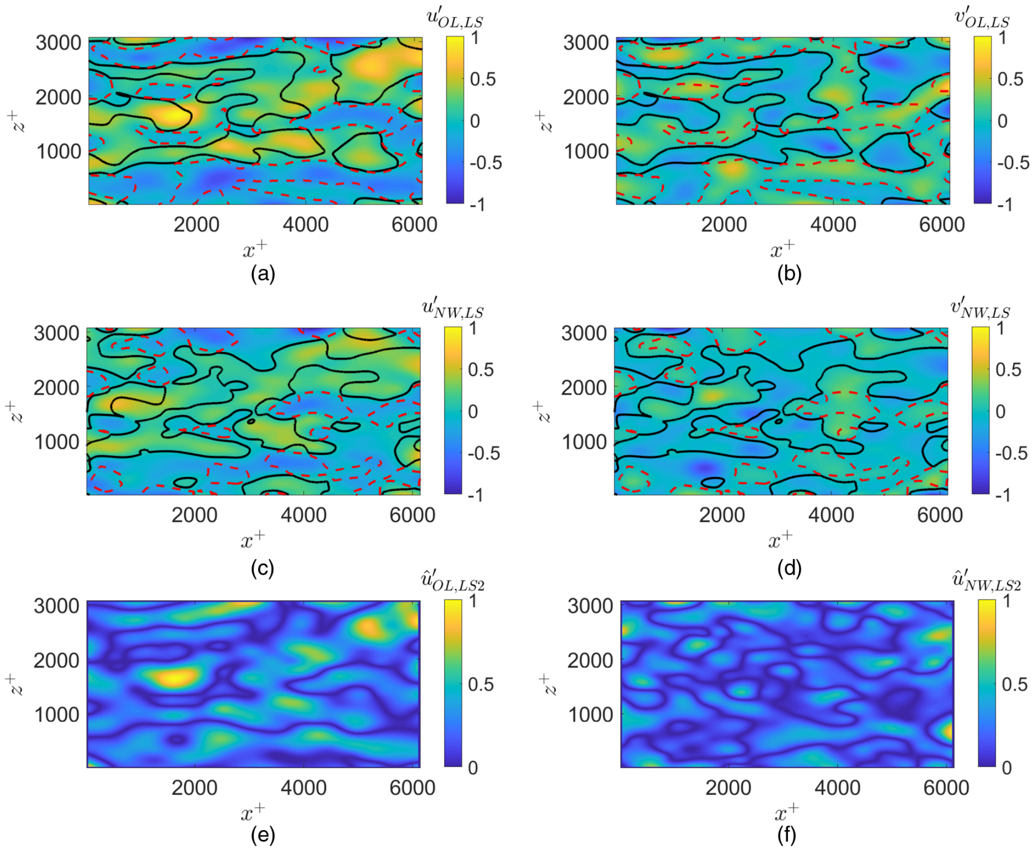

FIG. 6. Large-scale streamwise and wall-normal velocity fluctuations (a) $u'_{\mathrm{OL,LS}}$, (b) $v'_{\mathrm{OL,LS}}$, (c) $u'_{\mathrm{NW,LS}}$, (d) $v'_{\mathrm{NW,LS}}$ and amplitudes (e) $\hat{u}'_{\mathrm{OL,LS2}}$, (f) $\hat{u}'_{\mathrm{NW,LS2}}$ at $\{y^+_{\mathrm{NW1}} = 1, y^+_{\mathrm{OL}} = 123\}$ and $t^+ = 36$. Black solid lines indicate large-scale sweeps and red dashed lines large-scale ejections.

different scales drawn from other studies. This should be substantiated by a detailed interpretation of each IMF according to its inherent scales as stated by Huang *et al.* [37] for turbulent time series using a single-dimension EMD and by Cheng *et al.* [38] based on a 2D univariate EMD. This is, however, beyond the scope of the current investigation, which primarily focuses on the large scales.

### B. Instantaneous results

The large-scale streamwise and wall-normal velocity fluctuations as well as the large-scale amplitudes at $\{y^+_{\mathrm{NW1}} = 1, y^+_{\mathrm{OL}} = 123\}$ are shown in Fig. 6 for $t^+ = 36$, i.e., the same time step as discussed in Sec. IV A. The velocity fluctuations are normalized to lie in the interval $[-1, 1]$ and the amplitudes in $[0, 1]$ such that the data can be easily compared between the inner and the outer layer. The areas of bursting activity are marked by black solid lines for sweeps and red dashed lines for ejections in Figs. 6(a)–6(d).

This time step possesses a high correlation between inner and outer layer with maximum values of $R_{S,\max} = 0.68$ for the superposition, $R_{\mathrm{sw,max}} = 0.46$ for the sweeps, $R_{\mathrm{ej,max}} = 0.52$ for the ejections, and $R_{\mathrm{AM,max}} = 0.66$ for the amplitude modulation. The complete correlation maps for all phenomena are illustrated in Fig. 7. Due to the large-scale nature of the investigated events, the correlation map usually consists of a broad area of high correlation stretched in the streamwise direction rather than a sharp peak. For the bursts, this area is typically less distinct than for the

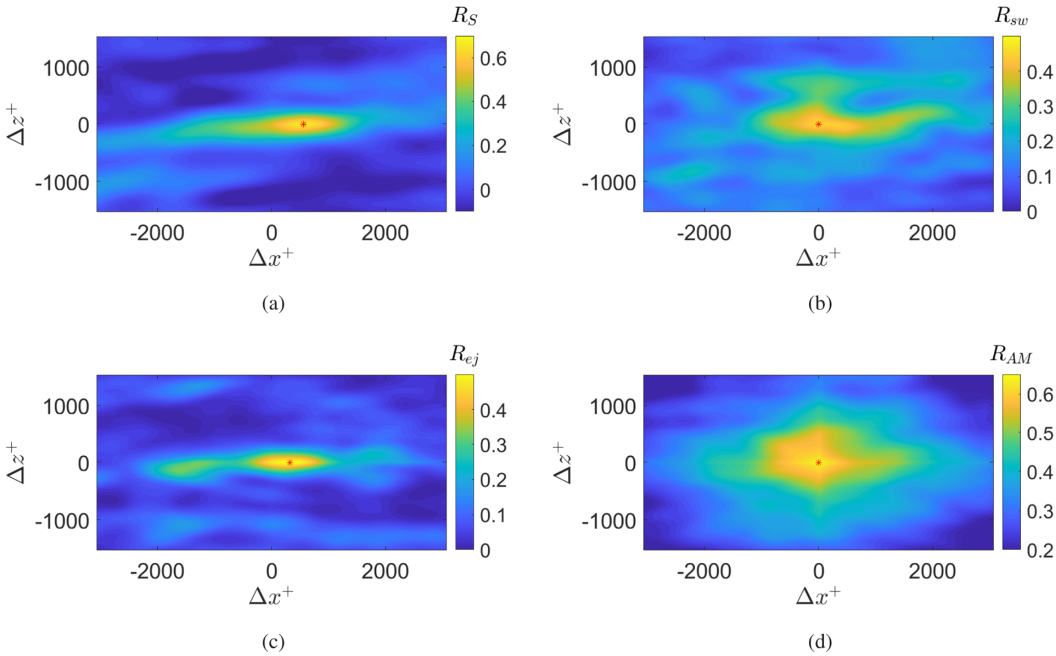


FIG. 7. Correlation maps of (a) superposition $R_S$, (b) sweeps $R_{\text{sw}}$, (c) ejections $R_{\text{ej}}$, and (d) amplitude modulation $R_{\text{AM}}$ for the same data as in Fig. 6.

superposition. With decreasing inner-outer correlation, secondary areas of medium-high correlation might occur as visible in Figs. 7(b) and 7(c). This primarily applies to the bursting events, probably caused by their short and localized life time.

Regarding the amplitude modulation, the near-wall amplitude approaches zero more often than the outer-layer amplitude, i.e., on average, the near-wall scales appear to be shorter, but overall, similarities can be observed, e.g., within the elevated areas around $x^+ > 2000$, $z^+ \approx 500$ and in the upper right region. This impression is confirmed by the correlation coefficient of $R_{\text{AM,max}} = 0.66$. The positions of maximum correlation, which are marked by a red star in Fig. 7, yield inclination angles of $\Theta_S = 12.50°$, $\Theta_{\text{sw}} = 90.00°$, $\Theta_{\text{ej}} = 21.00°$, and $\Theta_{\text{AM}} = 90.00°$. By convention, an angle of $90°$ indicates zero displacement between the inner and the outer layer. The superposition and the ejections are characterized by positive angles, i.e., the outer-layer structures lead the near-wall structures. It is shown in Fig. 7 that the spanwise shifts between the inner and the outer layer are very small. Thus, the inclination angles primarily result from streamwise shifts.

The instantaneous findings show that all interaction phenomena can be detected very well based on the spatial large-scale features determined by the 2D NA-MEMD. We can also conclude that the approach for the amplitude modulation investigation presented in Ref. [6] for pointwise temporal signals is perfectly suited for 2D spatial data.

### C. Time-dependent quantities

Since the present approach applies a spatial inner-outer interaction analysis, the temporal evolution of the involved quantities can be studied. In Fig. 8, the time-dependent maximum correlation coefficients of all phenomena are shown for both near-wall positions. High-frequency fluctuations are removed by applying a moving average filter with a window size of 10 time steps, i.e., $\Delta t^+ = 32.5$. As an example, the unfiltered distribution of the superposition is shown in grey. The amplitude modulation is the strongest interaction phenomenon with the least temporal fluctuations at both near-wall positions. Thus, the large-scale amplitude variations are most dominant as well

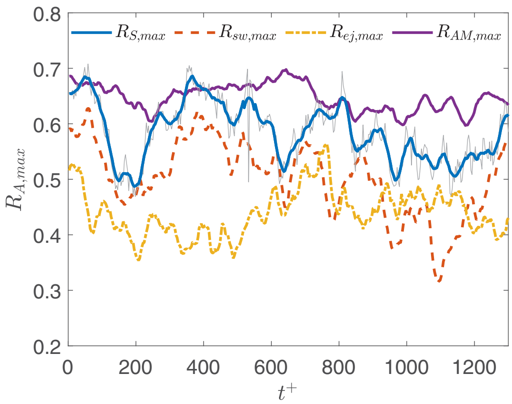


(a)

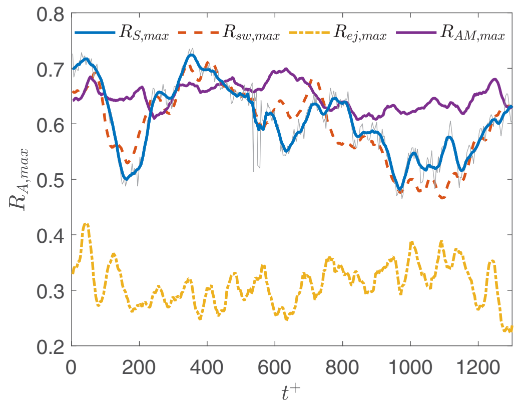


(b)

FIG. 8. Time-dependent maximum correlation coefficients at (a) $y^+_{\mathrm{NW1}} = 1$ and (b) $y^+_{\mathrm{NW1}} = 5$.

as coherent across all wall-normal layers and in time. The correlation of the ejections yields the smallest values, i.e., ejections play only a minor role in the interaction cycle. On average, the correlation with respect to the superposition $R_{S,\max}$ is nearly alike at both near-wall locations. The distributions of the sweeps' correlation roughly follow the trends of $R_{S,\max}$ with an offset of its mean to smaller values at $y^+_{\mathrm{NW1}} = 1$. This behavior shows that the similarity between inner and outer large scales—expressed by $R_{S,\max}$—is primarily imposed by the sweeping motions at $y^+_{\mathrm{NW5}} = 5$. However, not all outer-layer sweeps are able to reach the direct vicinity of the wall with the same intensity, which reduces $R_{\mathrm{sw},\max}$ at $y^+_{\mathrm{NW1}} = 1$.

Note that we provide results of the inner-outer interaction at $\{y^+_{\mathrm{NW1}} = 1, y^+_{\mathrm{OL}} = 123\}$ using a univariate 2D EMD, which separately decomposes the inner- and the outer-layer data, in Appendix B. The correlations are severely reduced, which is caused by the scale misalignment between inner and outer large scales and among streamwise and wall-normal fluctuations. They also vary strongly in time, which results from a time-dependent variation of the range of scales assigned to the large scales. The discussion in Appendix A 4 concerning the difference of the IMFs produced by a univariate EMD, a MEMD, and an NA-MEMD shows that it is obvious that the mode alignment property of the NA-MEMD massively improves the findings of the interaction analysis. This justifies its increased mathematical complexity and its higher computational effort. Hence, if spatial data are available, the MEMD should be preferred over the univariate EMD.

The time-dependent inclination angles of all phenomena are given in Fig. 9. The quantities are filtered by a moving average similar to that of the correlation coefficients. The removed high-frequency variations mainly result from small shifts of the positions of the correlation peaks within the broad areas of high correlation shown in Fig. 7. However, the inclination angles still fluctuate strongly in time, which is more pronounced at $y^+_{\mathrm{NW5}} = 5$. This evidences that a simple averaged angle does not reflect the complex physics. Mostly, the angles indicate leading outer-layer large scales expressed by a positive angle, whereas the bursting events occasionally feature leading near-wall structures. The amplitude modulation has by far the largest inclination angles, which means that the near-wall and the outer-layer amplitudes only possess a small streamwise displacement. Recall that $\Theta = 90^\circ$ indicates zero displacement between the inner and the outer field. The varying distributions among all interaction phenomena reveal that the mechanism of interaction differs depending on the flow features.

Next, the cardinality of positive large-scale fluctuations with respect to the cardinality of all large-scale fluctuations defined by

$$n(t) = \frac{\mathrm{card}[u'_{\mathrm{LS}}(t) > 0]}{\mathrm{card}[u'_{\mathrm{LS}}(t)]} \tag{6}$$

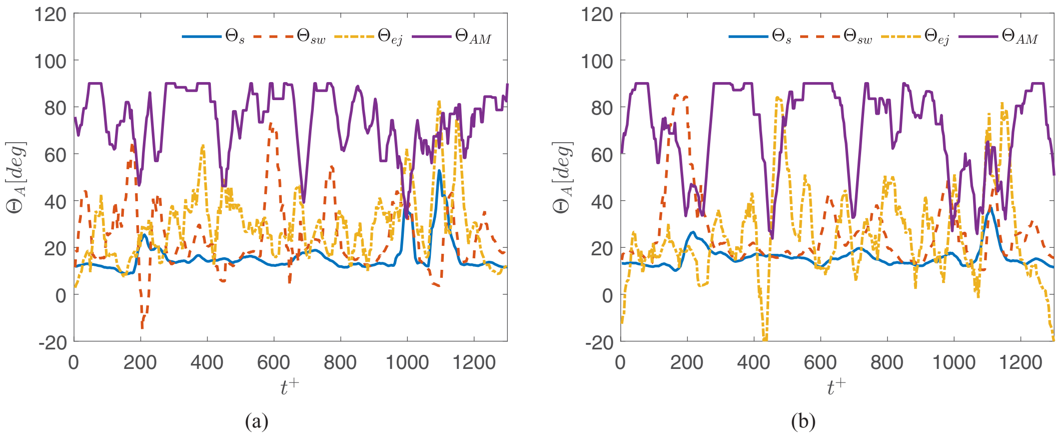


FIG. 9. Time-dependent inclination angles at (a) $y^+_{\mathrm{NW1}} = 1$ and (b) $y^+_{\mathrm{NW1}} = 5$.

is used to more thoroughly understand the large-scale trends inherent to the time-dependent maximum correlation coefficients and inclination angles. This cardinality ratio $n$ is basically a probabilistic measure to assess if either high-speed ($n > 50\%$) or low-speed ($n < 50\%$) large-scale structures are predominantly responsible for the near-wall imprint. Thus, it accounts for the global time-dependent profiles of the interaction quantities. In contrast to the skewness, which similarly measures asymmetry and is occasionally used in other studies [39,40], it offers a straightforward interpretation of the values as it does not involve a third power within its calculation.

The cardinality ratio is calculated independently for the near-wall and the outer-layer large scales as a function of time $t$. It is shown in Fig. 10(a) for the data at $y^+_{\mathrm{NW5}} = 5$ ($n_{\mathrm{NW}}$) and $y^+_{\mathrm{OL}} = 123$ ($n_{\mathrm{OL}}$). At both positions, the rates feature a slightly decreasing trend in the first half of the studied time frame. This is followed by a rapid reduction around $750 \leqslant t^+ \leqslant 1000$ with a subsequent strong increase. This behavior is easily explained by visualizations of the involved large scales, which are shown in a movie provided in the Supplemental Material [41]. In the outer layer, a large high-speed structure with two shorter adjacent positive large scales moves through the field of view for $t^+ \leqslant 750$. The following low-speed structure with a streamwise extent of $x^+ \approx 4000$ dominates the domain up to $t^+ \approx 1000$, which explains the strong degradation of $n_{\mathrm{OL}}$ in this area. The subsequent

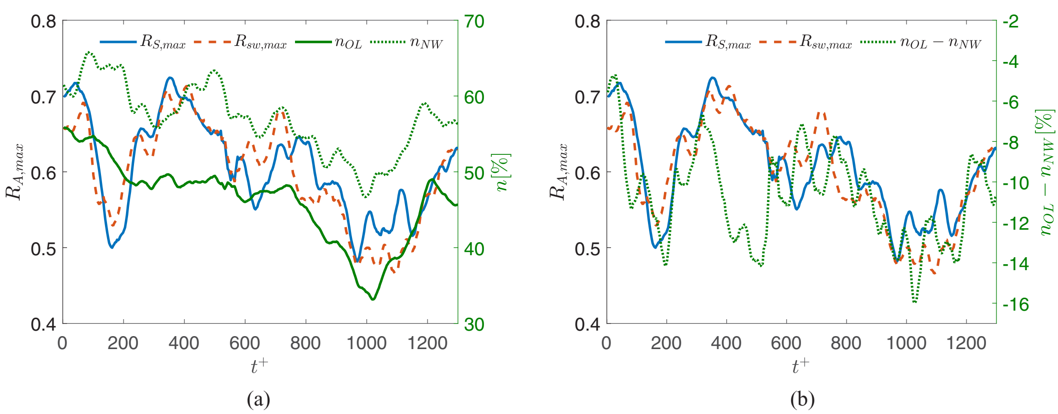


FIG. 10. Interdependence of correlation coefficients of superposition $R_{S,\max}$ and sweeps $R_{\mathrm{sw},\max}$ with (a) percentage of positive large scales $n$ and (b) percentage difference $n_{\mathrm{OL}} - n_{\mathrm{NW}}$ at $\{y^+_{\mathrm{NW5}} = 5, y^+_{\mathrm{OL}} = 123\}$.

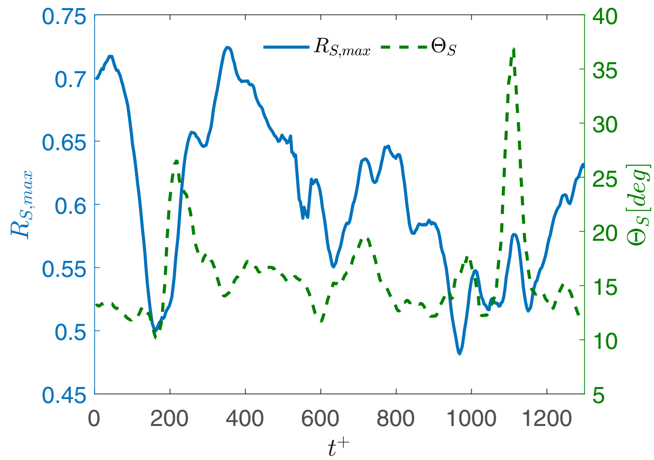


FIG. 11. Interdependence of correlation coefficients and inclination angles at $\{y^+_{\mathrm{NW5}} = 5, y^+_{\mathrm{OL}} = 123\}$ for the superposition phenomenon.

increase of $n_{\mathrm{OL}}$ can be traced back to two developing high-speed structures. However, their rather short lengths of $x^+ \approx 2000$ prevent an increase of $n_{\mathrm{OL}}$ up to the value from the beginning of the time series. Similar observations with a small temporal offset are made for the near-wall large scales and $n_{\mathrm{NW}}$.

The correlation coefficients for the superposition and the sweeps are also shown in Fig. 10(a). Besides their high-amplitude fluctuations, the distributions follow the global tendencies given by the fluctuation rates. Thus, generally speaking, the correlation between inner and outer large scales, i.e., the superposition, reduces (increases) as the amount of positive large-scale fluctuations decreases (increases). This is likely to be accompanied by reduced (enhanced) sweeping activity, which lowers (increases) the possibility of high-momentum fluid to reach the near-wall region and thus, the top-down communication. The observed behavior indicates that positive large scales are more "successful" in maintaining the inner-outer relation. This explains why Abbassi *et al.* [42] yielded a higher drag reduction when influencing the outer-layer high-speed large scales compared to the low-speed large scales.

Figure 10(b) additionally shows that $R_{S,\max}$ and $R_{\mathrm{sw},\max}$ are higher when the cardinality ratios of the near-wall and the outer-layer location are closer together, i.e., small values of $n_{\mathrm{OL}} - n_{\mathrm{NW}}$, and vice versa for small correlation coefficients except for the region $350 \leqslant t^+ \leqslant 550$. Of course, a higher similarity of the cardinality ratios increases the chance of more similar flow fields but it is not a necessary consequence.

There is a relation between the correlation coefficient and its associated inclination angle. This is exemplarily shown for the superposition at $\{y^+_{\mathrm{NW5}} = 5, y^+_{\mathrm{OL}} = 123\}$ in Fig. 11. With occasional deviations and minor temporal offsets, the distributions show an opposite behavior, which is confirmed by a minimum correlation coefficient of $R = -0.95$ at zero offset. In view of the former findings, this is not surprising. Since $R_{S,\max}$ is reduced with increasing dominance of low-speed large scales, the averaged outer-layer large-scale flow is slower for small $R_{S,\max}$. Thus, the velocity difference to the near-wall flow field is decreased, which results in a high inclination angle. Note that the inclination angle is $90^\circ$ when the inner and the outer field are not displaced.

The discussion of the time-dependent quantities shows that the maximum correlation coefficients and inclination angles of all phenomena feature severe temporal fluctuations, which could not have been detected by pointwise temporal data. The results indicate that the large-scale time-dependent behavior is determined by the rate of positive, i.e., high-speed, large scales to the total large-scale fluctuations at the inner and the outer layer and the difference between these rates.

TABLE III. Maximum correlation coefficients and inclination angles for 0D and 2D analysis. The 2D results are averaged over all 400 time steps.

| | | $R_{S,\max}$ | $\Theta_S$ | $R_{\mathrm{sw},\max}$ | $\Theta_{\mathrm{sw}}$ | $R_{\mathrm{ej},\max}$ | $\Theta_{\mathrm{ej}}$ | $R_{\mathrm{AM},\max}$ | $\Theta_{\mathrm{AM}}$ |
|---|---|---|---|---|---|---|---|---|---|
| $y^+_{\mathrm{NW1}} = 1$ | 2D | 0.58 | 15.88° | 0.50 | 24.19° | 0.44 | 28.78° | 0.65 | 71.69° |
| | 0D | 0.33 | 7.69° | 0.39 | −78.89° | 0.70 | −13.33° | 0.78 | 87.19° |
| $y^+_{\mathrm{NW5}} = 5$ | 2D | 0.61 | 15.86° | 0.60 | 26.21° | 0.31 | 25.07° | 0.65 | 68.69° |
| | 0D | 0.36 | 8.49° | 0.42 | 11.04° | 0.65 | −9.64° | 0.75 | 87.10° |

### D. Comparison with 0D findings

In total, 400 time steps of the 2D multivariate data are used to study the inner-outer interactions between $\{y^+_{\mathrm{NW1}} = 1, y^+_{\mathrm{OL}} = 123\}$ and $\{y^+_{\mathrm{NW5}} = 5, y^+_{\mathrm{OL}} = 123\}$. The resulting time-averaged maximum correlation coefficients and inclination angles are given in Table III together with the findings of the 0D analysis. Note that the considered time interval is too short to provide fully statistically converged averaged quantities due to the limited time frame of the simulation. However, this is not the aim of the current study. The averaged values serve as a benchmark how the increase in information, i.e., the spatial domain, affects the conclusions drawn from the inner-outer interaction analysis compared to the 0D results when both approaches cover the same time interval.

For the 0D data, only one value is obtained for each parameter since the temporal dimension is the only dimension. Thus, the 0D outcomes already reflect the average interaction within the given time frame. For a detailed discussion of the 0D results, e.g., visualizations of the large scales, amplitudes, and correlation functions, the reader is referred to the studies by Mäteling *et al.* [6,30]. However, it has to be emphasized that the present quantitative 0D findings marginally deviate from the previously published 0D results since the former findings did not include the wall-normal velocity fluctuations and were derived based on less elaborate versions of the EMD method.

The 0D correlation peaks are lower for the superposition and the sweeps and higher for the ejections and the amplitude modulation than the 2D maxima independent from the near-wall position. The inclination angles obtained by the 0D approach are significantly smaller compared to the 2D results except for the amplitude modulation. The angles with respect to the bursting events even indicate opposite directions of interaction for both approaches. While the 2D results indicate a lead of the outer-layer large scales compared to their near-wall impact for all phenomena, the 0D data shows a leading near-wall flow field for the sweeps at $y^+_{\mathrm{NW1}} = 1$ and the ejections at both near-wall locations. Since the sweeps are characterized by a positive streamwise fluctuation, it is intuitive to assume that they follow the behavior of the superposition with leading outer-layer structures. Presumably, there is just not enough data, i.e., sweeping motion, captured by the 0D data to accurately determine the correct, physical relation between inner and outer sweeps due to their highly intermittent and localized behavior. The same holds for the correlation coefficients of the bursting events. Even for the 2D data set, time steps with a rather small correlation feature spurious secondary correlation peaks with respect to the bursts.

A longer time sequence, as it is usually obtained from HWA measurements, might yield a convergence of the 0D results to the 2D findings. Unfortunately, this hypothesis cannot be tested due to the limited time frame of the DNS data. However, in earlier 0D studies of the superposition inclination angles around $\Theta_S = 11 - 15^\circ$ were identified [43,44], which are closer to our 2D superposition results than the present 0D outcomes. This can be considered some evidence for the stated hypothesis with respect to the superposition. Nevertheless, the correlation coefficients in the literature are usually smaller for the considered near-wall locations, which indicates a more accurate characterization of the interaction by the spatial approach. Hence, it is fair to state that the 2D findings are expected to yield a more relevant description of the flow physics due to the massively higher amount of data, i.e., streamwise and spanwise information in addition to the temporal domain.

## V. CONCLUSIONS

The inner-outer interaction of large-scale structures in a turbulent channel flow is investigated using two-dimensional, time-dependent streamwise and wall-normal velocity fluctuations. Wall-parallel planes of the fluctuations at two near-wall positions within the viscous sublayer ($y^+_{\mathrm{NW1}} = 1$ and $y^+_{\mathrm{NW5}} = 5$) and at an outer-layer location featuring the most-energetic large-scale motions ($y^+_{\mathrm{OL}} = 123$) are considered. Near-wall and outer-layer data are simultaneously decomposed into small and large scales by a two-dimensional noise-assisted multivariate empirical mode decomposition. This approach ensures that the modal representations of all quantities possess similar spectra and are coherent in time. It enables an accurate intermode comparison, which is a key prerequisite for an accurate interaction analysis.

The influence of outer-layer large-scale motions on the near-wall dynamics is investigated with respect to the phenomena of superposition, bursts, i.e., sweeps and ejections, and amplitude modulation. Spatial correlations of the large-scale features show the degree of near-wall modulation, expressed by the correlation coefficients, and the inclination angles indicate the displacement between outer-layer large scales and their near-wall imprint. The approach is an adaptation of the zero-dimensional, i.e., no spatial data are included, temporal procedure introduced by Mäteling *et al.* [6] to the two-dimensional, spatial domain. The massively increased information about the flow field in the form of spatial data increases the accuracy of the analysis. The spatial extent enables an analysis of the meandering behavior of the large scales in the spanwise direction and supersedes Taylor's hypothesis. Hence, the temporal information can be used to study time-dependent features of the inner-outer interaction.

In summary, the two-dimensional multivariate approach has been implemented and the results confirm its superior performance compared to a scale separation by a two-dimensional univariate empirical mode decomposition. A comparison of the time-averaged results to the zero-dimension findings shows that solely time-dependent approaches are insufficient at predicting the degree of inner-outer coherence for all phenomena within the studied time frame. The inclination angles are clearly underestimated and can hardly be used even for qualitative findings. Especially the study of sweeps and ejections suffers from too limited data.

The correlation coefficients and inclination angles of the two-dimensional inner-outer interaction phenomena possess distinct temporal fluctuations, which shows that averaged values of these quantities are insufficient to describe the complex physical processes. These temporal variations relate to changes in the rate of high-speed large scales to the total large-scale fluctuations at the near-wall and the outer-layer location. This relation indicates that high-speed large scales are more relevant for the interaction cycle than slow-speed large scales. In addition, the inner-outer interaction is sensitive with respect to the difference of the cardinality ratios at the inner and the outer location.

Overall, the amplitude modulation represents the highest and the interaction by ejections the lowest contribution to the inner-outer interaction within the viscous sublayer. The differences between the two near-wall positions are determined by a reduced correlation of the ejections, an increased correlation of the sweeps, and increased variations among the inclination angles at $y^+_{\mathrm{NW5}} = 5$.

Finally, we emphasize that the 2D NA-MEMD approach possesses enormous potential in improving the knowledge about inner-outer interactions in a spatiotemporal framework. It can be used to extend and enhance existing models describing the near-wall modulation as introduced by, e.g., Marusic *et al.* [31] and Mathis *et al.* [44], for the time-dependent, single-point streamwise velocity fluctuations. The models will be able to accurately predict the near-wall behavior solely based on outer-layer data. This means easier access to the essential flow structures to manipulate the near-wall flow field in view of, e.g., drag reduction.

*Code availability.* A python implementation of the two-dimensional noise-assisted multivariate empirical mode decomposition is available at Ref. [45].

*Data availability.* The turbulent channel flow data are obtained from the Johns Hopkins Turbulence Databases available at Ref. [46].

## APPENDIX A: EXTENSIVE VIEW OF THE 2D NA-MEMD ALGORITHM

Section III A provides a high-level overview of the applied 2D NA-MEMD algorithm and detailed descriptions are given in this Appendix. A close look at the sifting process is taken in Appendix A 1, in which visualizations of the important steps are presented for an exemplary flow field. The stopping criterion applied during the sifting process is discussed in Appendix A 2. Appendix A 3 explains how the additional application-related NA-MEMD parameters, i.e., the number of projection directions and the noise properties, have been selected. Finally, we emphasize the advantageous properties of the NA-MEMD compared to an MEMD and a univariate EMD in Appendix A 4.

### 1. Detailed insight into the sifting process

The schematic diagram in Fig. 2 is complemented by visualizations of the most important parameters involved in the first iteration through the 2D NA-MEMD algorithm. The velocity fluctuations at $\{y^+_{\mathrm{NW1}} = 1, y^+_{\mathrm{OL}} = 123\}$ of the exemplary time step $t^+ = 36$, which is also used in Secs. IV A and IV B, are taken for this demonstration.

The input data, i.e., the four velocity fluctuations $u'_{\mathrm{OL}}, u'_{\mathrm{NW}}, v'_{\mathrm{OL}}, v'_{\mathrm{NW}}$ and the two noise channels, are shown in Fig. 12. They are stacked together to the 3D array $I$ in step I (see Fig. 2 for the step allocation). A projection onto unit projection vectors in step II yields the projected signals shown in Fig. 13 for the exemplary projection directions $k = 1, 7, 13, 19$. Note that the individual channels $l$ corresponding to the four velocity fields and the two noise channels are lost during this projection. However, depending on the projection direction, features of the individual velocity components are still visible. For example, Fig. 13(a) with $k = 1$ basically resembles the streamwise outer-layer fluctuations of Fig. 12(a) multiplied by minus one, while Fig. 13(c) with $k = 13$ is a combination of both outer-layer velocity components.

After determining the positions of extrema in the projected data (step III), an interpolation of the values of $I$ at these locations provides an upper and a lower surface envelope $e^{\varphi_k}_{l,\max}, e^{\varphi_k}_{l,\min}$ for each projection direction $k$ and each variate $l$ in step IV. Hence, the individual channels are regained. Visualizations of the envelopes are given in Fig. 14 for $k = 1$ and $l = 1, 4$ with the latter being related to $u'_{\mathrm{OL}}$ and $v'_{\mathrm{NW}}$. Note that, since the projection with $k = 1$ mainly resembles the negative streamwise outer-layer flow ($l = 1$), the lower envelope predominantly possesses positive and the upper envelope negative values, which might be counter-intuitive initially. The envelopes corresponding to the wall-normal near-wall data ($l = 4$) emphasize the strong events of this flow field.

The average of the upper and lower envelopes across all projection directions $M$ (step V) is shown in Fig. 15 for all four variates of the velocity data. These mean fields appear to be a somewhat unclear version of the input data $I$ shown in Fig. 12. Hence, their subtraction from $I$, which yields the detail $D$ in the last step, provides the smallest features inherent to the flow data. They are shown for all velocity variates in Fig. 16. The stopping criterion is used to determine if these pseudo-IMFs possess the characteristic IMF properties or if another sifting needs to be performed with the renewed input data $I - D$.

### 2. The stopping criterion

#### *a. Classical stopping criterion*

The choice of the stopping criterion is crucial for the outcome of the decomposition. Since a proper definition of the inherent extrema is missing, the condition for equality of the number of extrema and zero crossings that is used in the original formulation of the EMD algorithm cannot be applied for multivariate signals. Therefore, Rehman and Mandic [17] introduced an alternative formulation that we extended to 2D. The stopping criterion consists of two parts that have to be fulfilled for continuing the sifting process. The first condition takes into account the difference of the upper and lower surface envelopes in relation to the mean envelope and balances the challenging

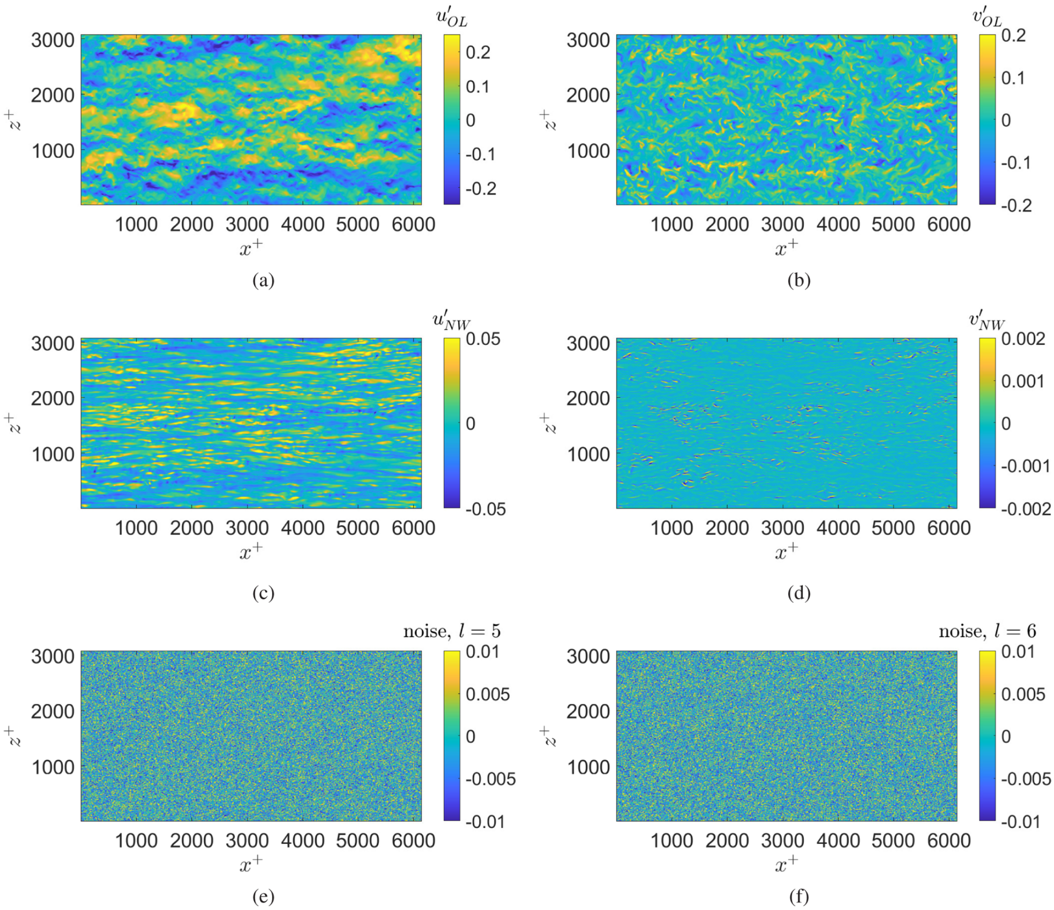


FIG. 12. Input data $I$, i.e., velocity fluctuations (a) $u'_{\mathrm{OL}}$, (b) $v'_{\mathrm{OL}}$, (c) $u'_{\mathrm{NW}}$, (d) $v'_{\mathrm{NW}}$ and (e), (f) Gaussian noise, at $\{y^+_{\mathrm{NW1}} = 1, y^+_{\mathrm{OL}} = 123\}$ and $t^+ = 36$.

compromise between over- and undersifting. It comprises two individual conditions and at least one of them has to be fulfilled. Mathematically, the first condition is defined by

$$\left\{\frac{1}{GH}\sum_{i=1}^{G}\sum_{j=1}^{H}[\Lambda(i,j) > \varepsilon_1]\right\} > \varepsilon_2 \quad \text{with} \quad \Lambda = \frac{\sqrt{\sum_{l=1}^{L} M_l^2}}{\sum_{k=1}^{K}\sqrt{\sum_{l=1}^{L}\left(e^{\varphi_k}_{l,\min} - e^{\varphi_k}_{l,\max}\right)^2}}, \tag{A1}$$

with $G, H$ being the number of pixels in the first and second dimension that fulfill the $\varepsilon_1$ threshold. Broadly speaking, $\Lambda$ represents the ratio of the mean envelope to the area enclosed by the upper and lower envelopes in an averaged manner, i.e., across all variates and projection directions. Thus, it indicates how symmetric the upper and lower envelopes are arranged around the zero axis, which is of utter importance since the IMFs are typically zero-mean modes. The stopping criterion checks how many locations possess rather high $\Lambda$ values with $\Lambda > \varepsilon_1$, i.e., $G + H$ locations, and compares their average value to the threshold value $\varepsilon_2$. The sifting proceeds if this mean value is larger than $\varepsilon_2$ to rearrange the envelopes more symmetric around zero.

The second part of the first stopping criterion catches outliers and is defined by any $[\Lambda(i, j) > \varepsilon_3]$. As long as the ratio of the mean envelope to the enclosed area is greater than $\varepsilon_3$ at at least one single position, the sifting continues to eliminate the outlier(s).

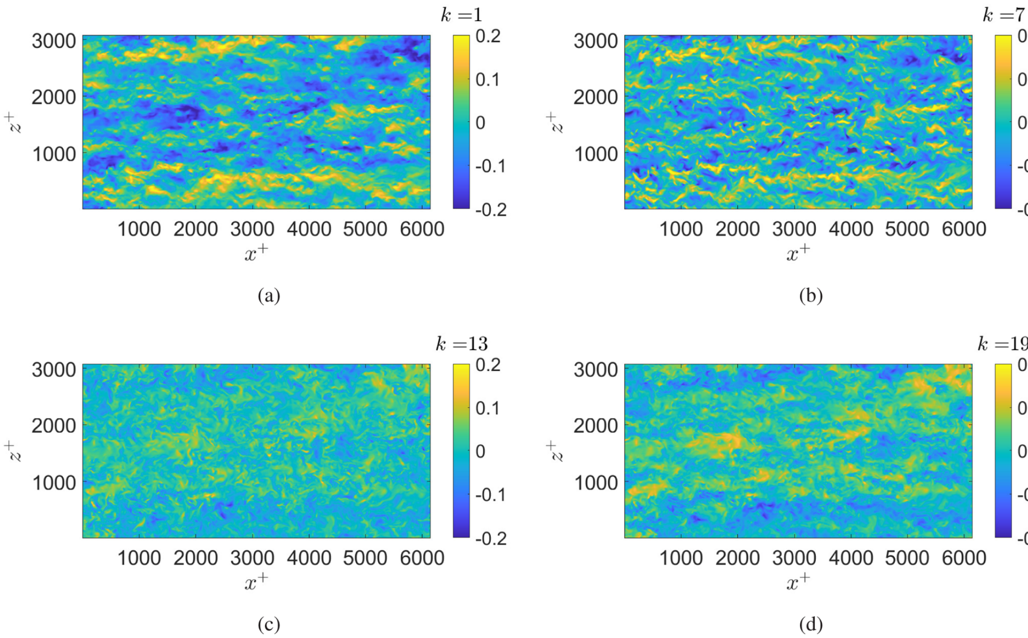


FIG. 13. Projections $P^{\varphi_k}$ of $I$ with exemplary projection directions (a) $k = 1$, (b) $k = 7$, (c) $k = 13$, and (d) $k = 19$ (step II in Fig. 2).

The second stopping criterion examines the number of extrema and allows the continuation of the sifting process as long as at least one projection direction possesses at least three extrema. This ensures that the IMF does not end up as a monotonic function.

### *b. Adaptation to present problem*

The described stopping criterion possesses two major challenges. The obvious difficulty is the choice of appropriate threshold values $\varepsilon_1, \varepsilon_2, \varepsilon_3$. The second issue arises from the specific application. Since the flow fields are decomposed for each individual time step, the physical relation between subsequent flow fields is not automatically considered. Although the noise-assistance ensures that the IMFs always contain a similar range of scales, the energy associated with these scales might vary. To a large extent, this can be prevented by specifying the number of sifting operations conducted to determine the IMFs. The idea of replacing the traditional stopping criterion by a preset number of sifting operations was suggested by Wu and Huang [47]. Although the context differs, it is a well-suited approach for the current application. To a certain extent, it enables the control of the amplitudes of the IMFs since the number of sifts defines how much the upper and lower envelopes are balanced around the mean. Prescribing this number across the decomposition of all time steps ensures that equal-indexed IMFs of different time steps possess a comparable energy content. In combination with the noise assistance, which imposes a constrained range of scales of each IMF, each mode appears continuous in time although the data is individually decomposed for each time step. Of course, this requires a comparable total energy content of the original velocity data and no severe variation of the energy distribution among all scales but this assumption should be valid for the studied canonical turbulent flow. Nevertheless, we cannot define the number of sifting operations arbitrarily since the modes should still fulfill the typical IMF characteristics. Thus, confidence intervals are determined from the classical stopping criterion and define the boundaries for the IMF components obtained with fixed sifts.

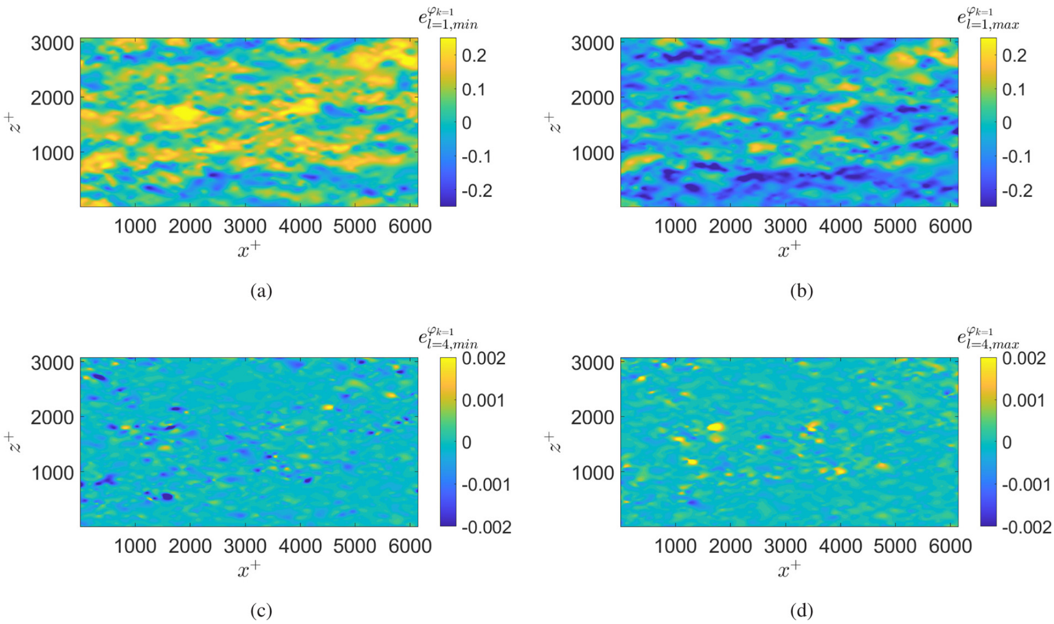


FIG. 14. Lower surface envelopes $e^{\varphi_k}_{l,\min}$ with (a) $l = 1$, (c) $l = 4$ and upper surface envelopes $e^{\varphi_k}_{l,\max}$ with (b) $l = 1$, (d) $l = 4$ based on extrema of $P^{\varphi_k}$ with $k = 1$ (step IV in Fig. 2).

To tackle the addressed issues, we first applied ten combinations of the three threshold levels, which are listed in Table IV and vary around the standard values suggested by Rehman and Mandic [17], i.e., $\varepsilon_1 = 0.01,\ \varepsilon_2 = 0.01,\ \varepsilon_3 = 0.1$. They are used to define confidence limits for

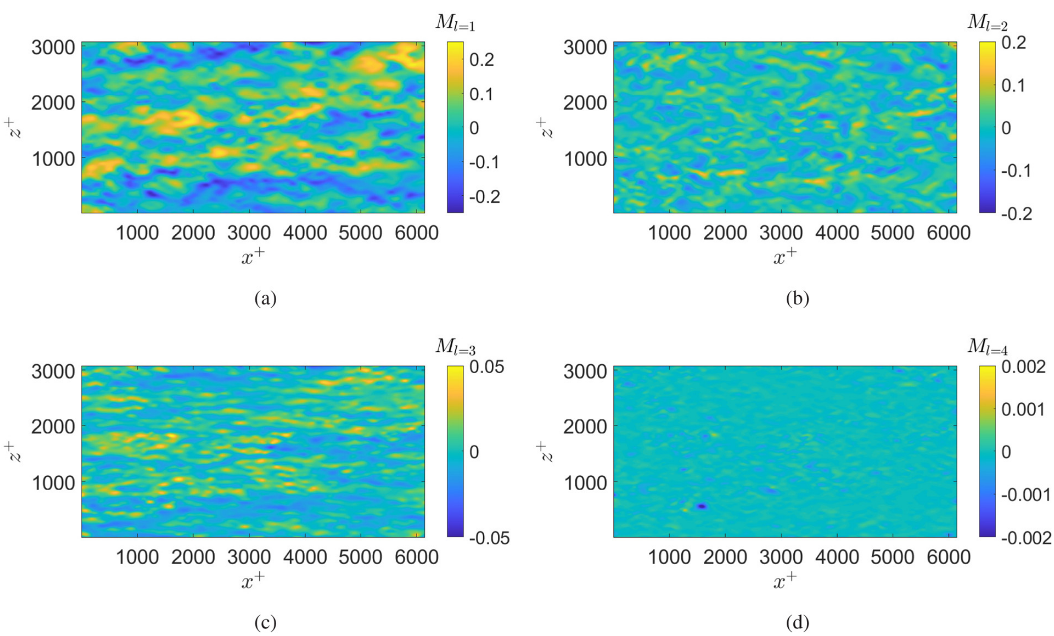


FIG. 15. Mean surface envelopes $M_l$ with (a) $l = 1$, (b) $l = 2$, (c) $l = 3$, and (d) $l = 4$ (step V in Fig. 2).

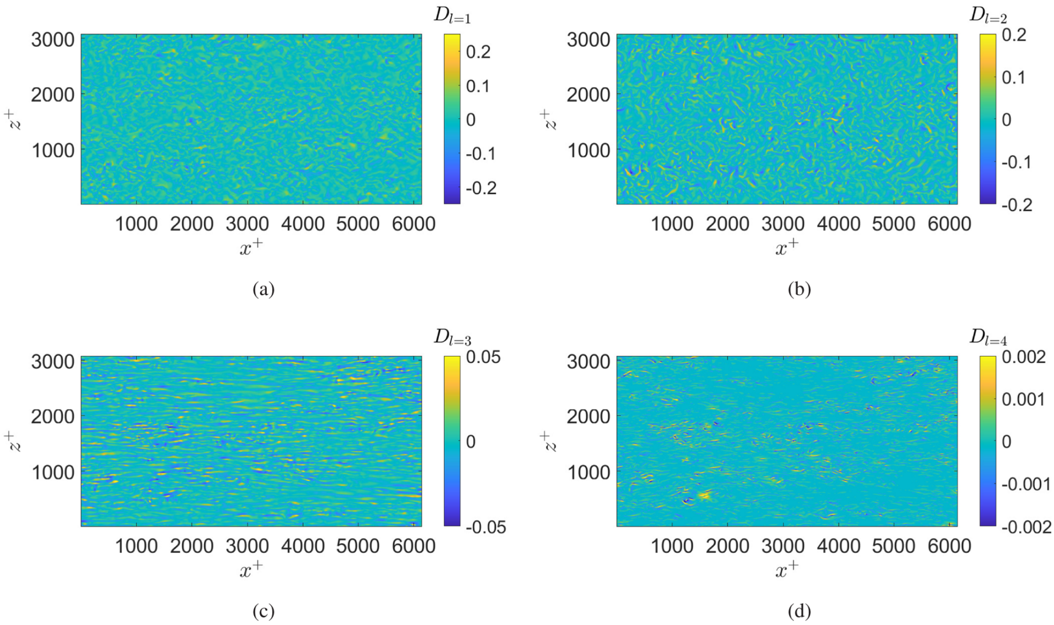


FIG. 16. Detail $D_l$ with (a) $l = 1$, (b) $l = 2$, (c) $l = 3$, and (d) $l = 4$ (step VI in Fig. 2).

each IMF component as outlined by Huang *et al.* [48] for the single-dimension EMD. Note that these confidence limits are determined individually for each time step and serve the purpose of indicating a valid range of IMF properties. This is in contrast to all other confidence limits used during the manuscript, which are calculated across the temporal domain and thus, reveal variations over time.

For each IMF number, each variate, and each time step, the mean and the standard deviation are determined across all configurations of stopping criteria. For the upper 95% confidence limit, two standard deviations are added to the mean IMF, while two standard deviations are subtracted from the mean to determine the lower bound. Next, a fixed number of sifts per IMF is specified, i.e., it is defined how many iterations are performed to determine each IMF without considering the previously applied stopping criteria. For the current investigation, the combination of five sifts for the first IMF and four sifts for each of the subsequently determined IMFs yields modes within the identified 95% confidence intervals. For brevity, the individual IMFs and the respective confidence limits are not shown. Instead, the premultiplied streamwise energy spectra and their corresponding confidence limits are presented in Fig. 17 since they clearly show the information of interest at a glance. The spectra given in Fig. 17 are calculated using the streamwise large scales at $\{y^+_{\mathrm{NW1}} = 1, y^+_{\mathrm{OL}} = 123\}$ and $t^+ = 36$. It is obvious how well they are located within the confidence intervals. In addition, although the energy content varies by about one order of magnitude, the shape of the spectra and the inherent range of streamwise and spanwise wavelengths is nearly identical. Again, this demonstrates the excellent mode alignment across different variates enabled by the applied decomposition strategy.

TABLE IV. Combinations of stopping criteria to determine the confidence limits of the IMFs.

| | | | | | | | | | | |
|---|---|---|---|---|---|---|---|---|---|---|
| $\varepsilon_1$ | 0.02 | 0.015 | 0.01 | 0.01 | 0.01 | 0.01 | 0.01 | 0.015 | 0.015 | 0.01 |
| $\varepsilon_2$ | 0.01 | 0.01 | 0.01 | 0.02 | 0.015 | 0.01 | 0.01 | 0.01 | 0.015 | 0.015 |
| $\varepsilon_3$ | 0.1 | 0.1 | 0.1 | 0.1 | 0.1 | 0.2 | 0.15 | 0.15 | 0.15 | 0.15 |

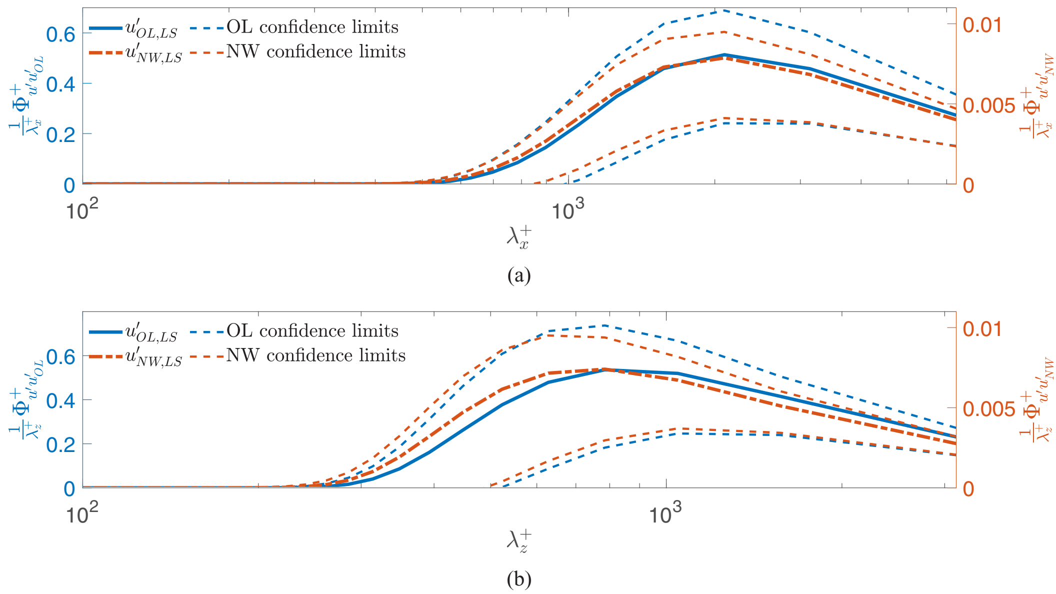


FIG. 17. Premultiplied streamwise energy spectra $\frac{1}{\lambda^+}\Phi^+_{u'u'}$ of the near-wall and the outer-layer large scales at $\{y^+_{\mathrm{NW1}} = 1, y^+_{\mathrm{OL}} = 123\}$ and $t^+ = 36$ in the (a) streamwise and (b) spanwise direction.

Note that fixing of the number of sifts is meaningless in the 0D approach and the standard values for the stopping criteria are applied.

### 3. Discussion of the selected decomposition parameters

#### *a. Noise properties*

Applying a noise-assisted MEMD algorithm requires the preset of the noise properties. As outlined in Sec. III A, two channels with random Gaussian noise are appended to the flow data prior to decomposition. The inherent noise power is defined to be 2% of the variance of the flow data with zero mean. The variance of the flow data is determined across all four velocity components, i.e., $u'_{\mathrm{OL}}$, $u'_{\mathrm{NW}}$, $v'_{\mathrm{OL}}$, $v'_{\mathrm{NW}}$, of the respective time step and is consequently re-calculated for each time step. A preceding parameter study using 40 consecutive time steps at $\{y^+_{\mathrm{NW1}} = 1, y^+_{\mathrm{OL}} = 123\}$ identified the appropriate number of noise channels, which was varied between 1, 2, 3, and the noise power. Following the recommendation of Rehman *et al.* [24] with respect to the single-dimension NA-MEMD, the tested noise power measured $\sigma^2_{\mathrm{noise}} = 2,\ 5,\ 10\%$ of the flow data's variance. The final decision was based on the properties of the reconstruction loss, the properties of the spectra of the IMFs, the visual impression with respect to their temporal evolution, and the efficiency. The latter has to be taken into account since an increasing number of noise channels significantly increases the computational cost.

The reconstruction loss is defined by the difference between the original data and the sum of all IMFs and should approach zero by definition. For all studied parameter configurations, the reconstruction loss is very similar. Depending on the velocity component, it is on the order of $\mathcal{O}(10^{-18}) - \mathcal{O}(10^{-20})$ and thus, negligibly small. We can conclude that the 2D NA-MEMD is energy-preserving, a result that has been shown for the time-dependent 0D EMD by, e.g., Singh *et al.* [49].

The time-averaged premultiplied streamwise energy spectra of all outer-layer IMFs are shown in Fig. 18 as a function of the streamwise wavelength for different noise variances and a different number of noise channels. Besides the temporal average, the standard deviation of each IMF number

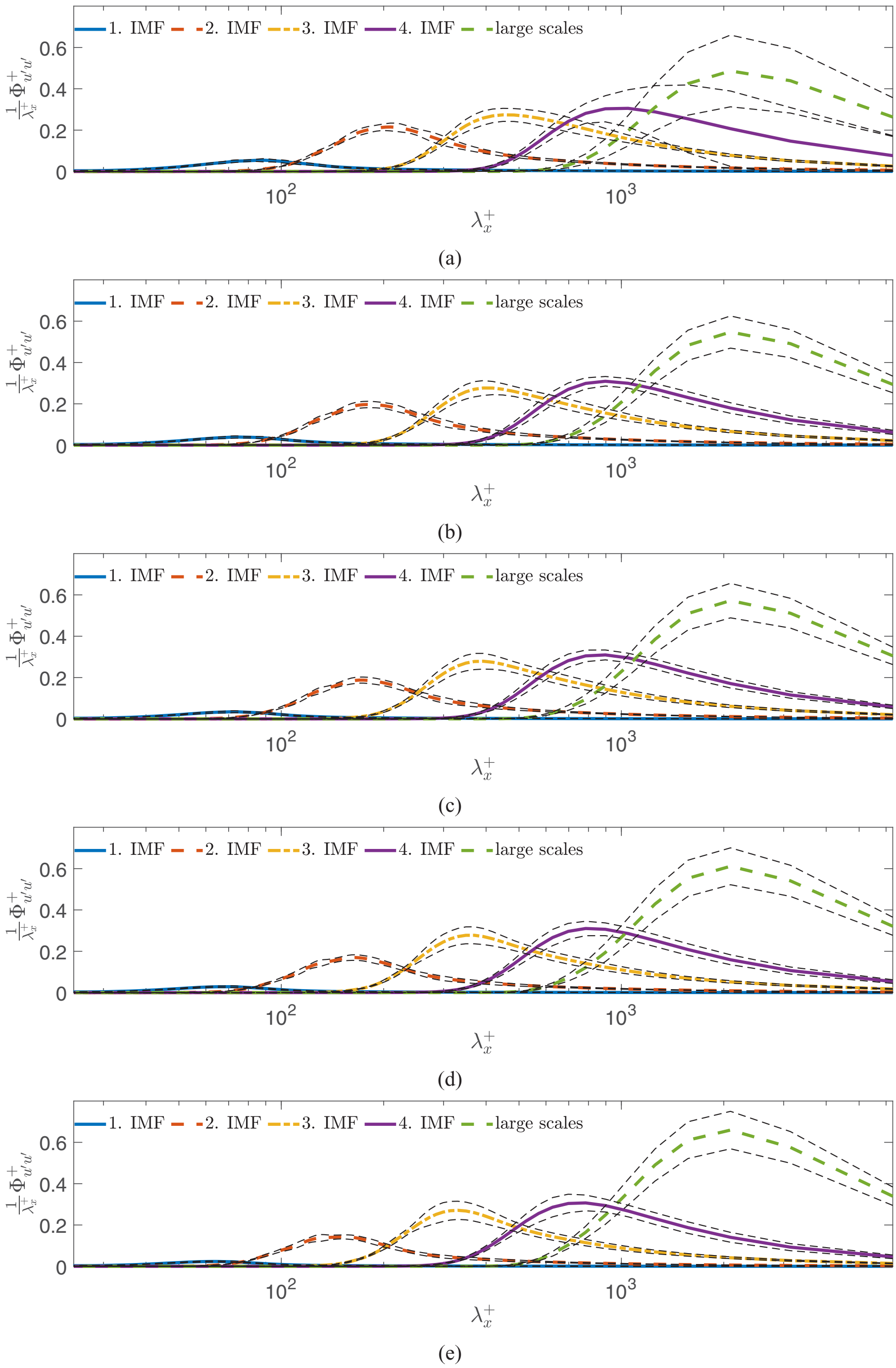


FIG. 18. Time-averaged premultiplied streamwise energy spectra $\frac{1}{\lambda_x^+}\Phi^+_{u'u'}$ of the outer-layer IMFs and 95% confidence limits (black dashed lines) as a function of the streamwise wavelength $\lambda_x^+$ with $\sigma^2_{\text{noise}} = 2\%$ and (a) one, (b) two, (c) three noise channels and with two noise channels and (d) $\sigma^2_{\text{noise}} = 5\%$, (e) $\sigma^2_{\text{noise}} = 10\%$.

TABLE V. Order of magnitude of the spatially and temporally averaged reconstruction loss for the data at $\{y^+_{\mathrm{NW1}} = 1, y^+_{\mathrm{OL}} = 123\}$ using the univariate EMD (uniEMD), the MEMD, and the NA-MEMD.

| | $u'_{\mathrm{OL}}$ | $v'_{\mathrm{OL}}$ | $u'_{\mathrm{NW}}$ | $v'_{\mathrm{NW}}$ |
|---|---|---|---|---|
| uniEMD | $\mathcal{O}(10^{-8})$ | $\mathcal{O}(10^{-18})$ | $\mathcal{O}(10^{-9})$ | $\mathcal{O}(10^{-15})$ |
| MEMD | $\mathcal{O}(10^{-9})$ | $\mathcal{O}(10^{-10})$ | $\mathcal{O}(10^{-10})$ | $\mathcal{O}(10^{-12})$ |
| NA-MEMD | $\mathcal{O}(10^{-18})$ | $\mathcal{O}(10^{-18})$ | $\mathcal{O}(10^{-19})$ | $\mathcal{O}(10^{-20})$ |

and each variate is calculated to define 95% confidence intervals. They are indicated by black dashed lines in Fig. 18. It is obvious from Fig. 18(a) that the usage of only one noise channel yields high temporal variations, i.e., broad confidence intervals, especially for the medium and large scales. The difference between two and three noise channels [Figs. 18(b) and 18(c)] is marginal, which indicates a convergence of the IMF properties. The value of the noise power influences the results only to a minor extent when using two noise channels. The confidence limits are slightly tighter for $\sigma^2_{\mathrm{noise}} = 2\%$. The same conclusions are drawn from the inspection of the spectra as a function of the spanwise wavelength and also for the other variates.

The findings coincide with the visual impression of the temporal coherence between consecutive IMFs (not shown). The usage of three instead of two noise channels has no significant influence on the IMF properties but increases the computational time by around 10%. Thus, two noise channels with a variance of 2% of the variance of the flow data are chosen. Note that for the sake of completeness, the influence of the noise parameters on the 0D results was also checked and the same trends as for the 2D data have been observed.

#### *b. Projection directions*

A parameter of choice when using a multivariate EMD approach is the number of projection directions. For both data sets, $K = 22$ projection directions are used. The 0D data set is insensitive to a variation of $K$, which was studied for values between $9 \leqslant K \leqslant 72$. For the 2D data, the investigation of 40 consecutive time steps at $\{y^+_{\mathrm{NW1}} = 1, y^+_{\mathrm{OL}} = 123\}$ showed a low influence. A small number of projection directions leads to minor mode mixing and occasionally reduced temporal coherence of the modes, while a large number increases the range of scales inherent to one IMF, i.e., the total number of IMFs decreases, and also the computational effort of the sifting process increases tremendously. Due to the slightly varying range of scales for different $K$, a comparison of the IMFs is not very useful. Hence, the results of the inner-outer interaction analysis are compared due to their significance for the present investigation. Varying $K$ in the range [3,46] shows that the outcome is converging for $K \geqslant 22$. Hence, the most meaningful results with the least computational effort are obtained by $K = 22$ and for consistency, this number of projection directions is also used for the 0D data set.

### 4. Comparison to other EMD approaches

In the introduction of Sec. III and in Sec. III A, we theoretically discussed the drawbacks of univariate EMD approaches for the current application and the advantages of a multivariate and specifically a noise-assisted multivariate EMD method. In this section, the theoretical arguments will be supported by quantitative comparisons of the modes resulting from a univariate EMD, an MEMD, and a NA-MEMD. The three methods are applied to the 2D flow data at $\{y^+_{\mathrm{NW1}} = 1, y^+_{\mathrm{OL}} = 123\}$ covering the complete time interval.

#### *a. Reconstruction loss*

The spatially and temporally averaged reconstruction losses are given in Table V for all four velocity components. Although the order of magnitude is quite small for all methods, an increasing

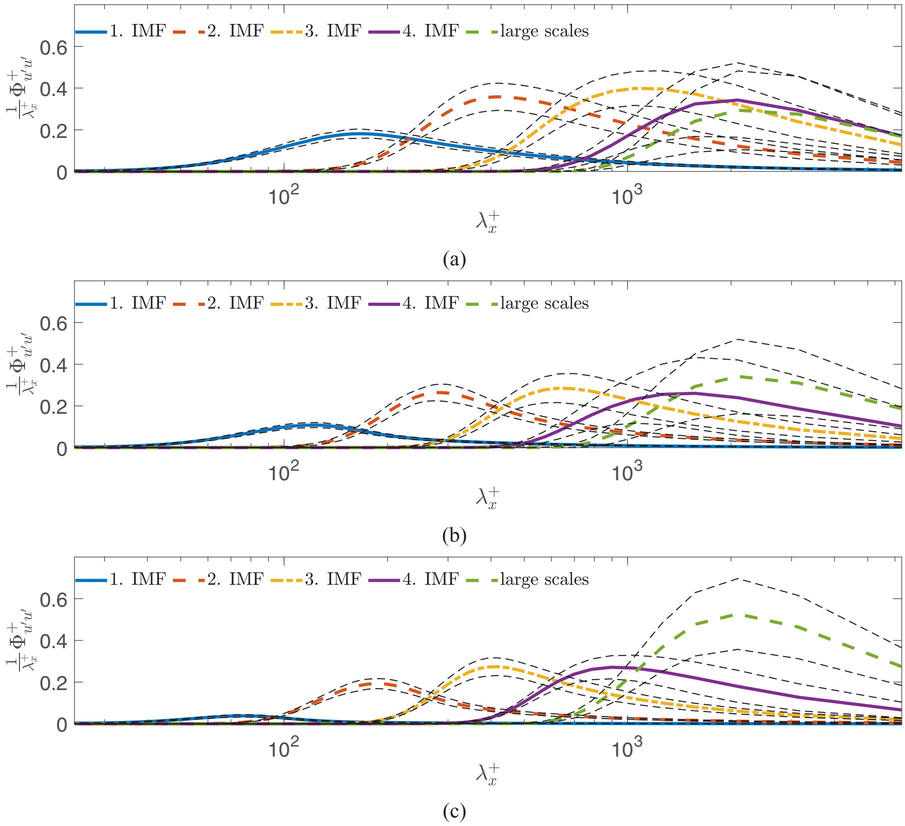


FIG. 19. Time-averaged premultiplied streamwise energy spectra $\frac{1}{\lambda^+}\Phi^+_{u'u'}$ of the outer-layer IMFs and 95% confidence limits (black dashed lines) as a function of the streamwise wavelength $\lambda_x^+$ obtained via the (a) univariate EMD, (b) MEMD, and (c) NA-MEMD.

complexity of the EMD algorithm clearly reduces the reconstruction loss. Using the univariate EMD, the error massively deviates between the velocity components and is much larger for the streamwise components. The difference is reduced when using a multivariate approach.

### *b. Energy spectra*

Time-averaged premultiplied streamwise energy spectra of the outer-layer IMFs and their 95% confidence intervals are shown in Fig. 19 as a function of streamwise wavelength. Severe mode mixing is observed for the fourth IMFs, i.e., medium-size scales, and the large scales when applying the univariate EMD and the standard MEMD. Although the overlapping area is reduced by the MEMD, a clear separation between the fourth IMF and the large scales is only obtained by using the NA-MEMD. In addition, Fig. 19(c) shows how the filter bank property deployed by the NA-MEMD enforces similar spectra with approximately doubled mean wavelengths of neighboring IMFs disregarding the varying energy content. The improved alignment of the range of scales inherent to each mode is certainly visible in the spectra of the MEMD compared to the univariate approach but a precise allocation is only achieved by the noise assistance.

The confidence intervals, which are indicated by black dashed lines in Fig. 19, become more narrow with increasing complexity of the algorithm, which is most obvious for the fourth IMFs and the large scales. This indicates that the temporal coherence between consecutive modes is best for the NA-MEMD, i.e., the comprised range of scales and the energy content of each IMF vary the least

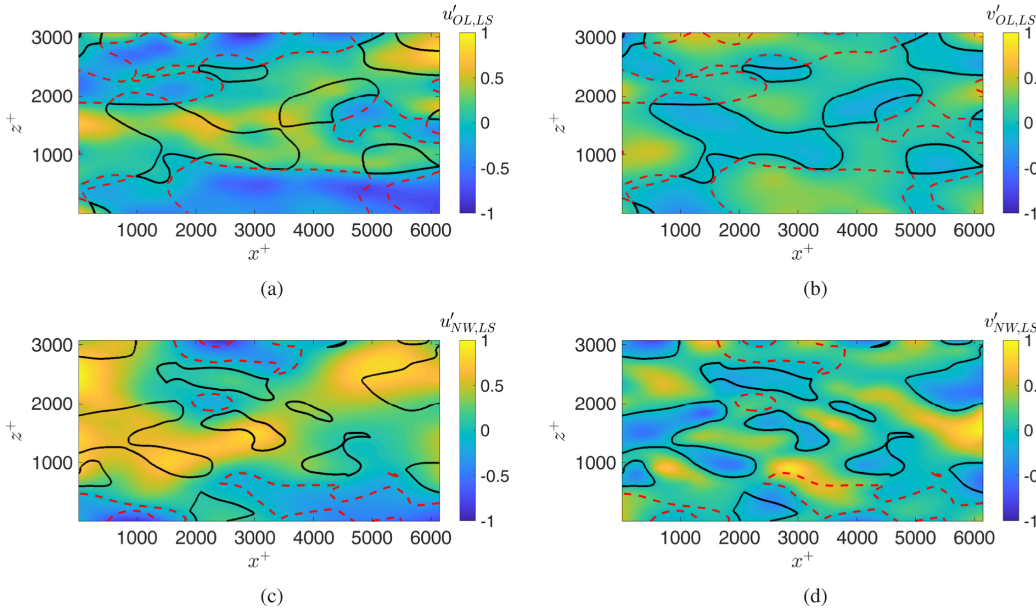


FIG. 20. Large-scale streamwise and wall-normal velocity fluctuations (a) $u'_{\mathrm{OL,LS}}$, (b) $v'_{\mathrm{OL,LS}}$, (c) $u'_{\mathrm{NW,LS}}$, and (d) $v'_{\mathrm{NW,LS}}$ at $\{y^+_{\mathrm{NW1}} = 1, y^+_{\mathrm{OL}} = 123\}$ for the same time step as in Fig. 6 using the univariate 2D EMD. Black solid lines indicate large-scale sweeps and red dashed lines large-scale ejections.

in time. A movie, which is provided in the Supplemental Material [50], showing the outer-layer and the near-wall large scales obtained by all three decomposition methods confirms this impression. We can thus conclude that the NA-MEMD provides the most physical modes and temporal changes are most likely due to physical processes rather than methodical bias. In addition, the movie clearly reveals an increasing relation between the near-wall and the outer-layer large scales when changing from a univariate to a multivariate decomposition strategy.

For conciseness, the spectra and the temporal evolution are not presented for all IMFs of all velocity components. However, the discussed differences between univariate EMD, MEMD, and NA-MEMD are evident in the other quantities as well. Thus, these findings show why the NA-MEMD is the most suited algorithm for scale separation in the context of inner-outer interaction analysis. In the next section, results of the interaction analysis obtained by using the univariate EMD further confirm this statement.

## APPENDIX B: INNER-OUTER INTERACTION ANALYSIS BASED ON UNIVARIATE EMD

In the following, results of the 2D inner-outer interaction analysis at $\{y^+_{\mathrm{NW1}} = 1, y^+_{\mathrm{OL}} = 123\}$ using the 2D univariate EMD, in which the four involved velocity fluctuations $u'_{\mathrm{OL}}, u'_{\mathrm{NW}}, v'_{\mathrm{OL}}, v'_{\mathrm{NW}}$ are separately decomposed, are presented. In contrast to applying the MEMD, the separate scale separation yields modal representations that do not contain the same range of scales across the different fluctuations. To compensate this mode misalignment as good as possible, a different number of IMFs is assigned to represent the outer-layer streamwise large scales $u'_{\mathrm{OL,LS}}$ compared to the large scales of the other fluctuations. Like in the NA-MEMD, modes greater than the fourth mode are summed to obtain $v'_{\mathrm{OL,LS}}, u'_{\mathrm{NW,LS}}, v'_{\mathrm{NW,LS}}$. For $u'_{\mathrm{OL,LS}}$, the sum of all modes greater than three is used.

Figure 20 shows the resulting large scales for the same time step as in Fig. 6, in which the large-scale fluctuations are obtained by the NA-MEMD. Although the best scale alignment is achieved by the chosen modal allocation, it is quite obvious that the different images do not

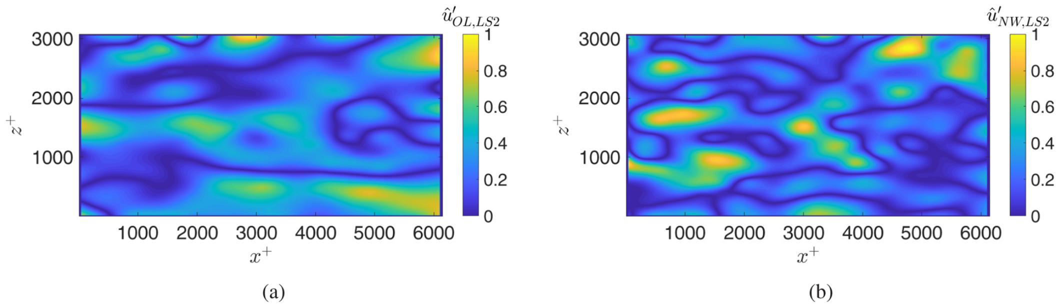


FIG. 21. Large-scale amplitudes of (a) the outer layer $\hat{u}'_{\mathrm{OL,LS}}$ and (b) the inner layer $\hat{u}'_{\mathrm{NW,LS}}$ for the same data as in Fig. 20.

comprise an equal range of scales. The scales of $u'_{\mathrm{NW,LS}}$ shown in Fig. 20(c) are very large, while $v'_{\mathrm{NW,LS}}$ in Fig. 20(d) contains comparatively small scales. Despite these fundamental deviations, we conduct the inner-outer interaction analysis to quantify the differences in the findings with respect to correlation coefficients and inclination angles.

For the exemplary time step shown in Fig. 20, the correlation coefficients possess maximum values of $R_{S,\mathrm{max}} = 0.52$ for the superposition, $R_{\mathrm{sw,max}} = 0.49$ for the sweeps, and $R_{\mathrm{ej,max}} = 0.53$ for the ejections. Compared to the NA-MEMD based values given in Sec. IV B, the correlation with respect to superposition is massively lowered while it is nearly equal for the bursting events. The large-scale amplitudes for the univariate scale separation are given in Fig. 21. Their maximum correlation measures $R_{\mathrm{AM,max}} = 0.64$, which is only slightly lower compared to the multivariate decomposition.

Next, the univariate approach is applied to all 400 time steps that are investigated in the multivariate analysis. The temporal distributions of the maximum correlation coefficients and the inclination angles, which are filtered by a moving average covering 10 time steps ($\Delta t^+ = 32.5$), are provided in Fig. 22 and the corresponding time-averaged quantities are presented in Table VI. For reference, the table additionally lists the time-averaged values based on the NA-MEMD analysis.

A comparison between Figs. 22(a) and 8(a) as well as the averaged values in Table VI reveal that a scale separation by the univariate approach yields smaller maximum correlation coefficients than

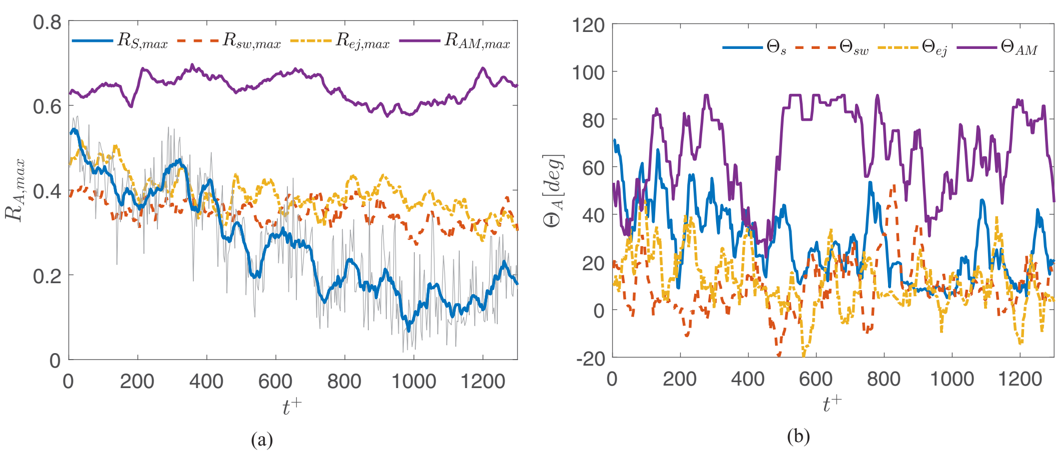


FIG. 22. Time-dependent (a) maximum correlation coefficients $R_{A,\mathrm{max}}$ and (b) corresponding inclination angles $\Theta_A$ at $\{y^+_{\mathrm{NW1}} = 1, y^+_{\mathrm{OL}} = 123\}$ using the univariate EMD.

TABLE VI. Maximum correlation coefficients and inclination angles at $\{y^+_{\mathrm{NW1}} = 1, y^+_{\mathrm{OL}} = 123\}$ using the univariate EMD (uniEMD) and the NA-MEMD. The results are averaged over all 400 time steps.

| | $R_{S,\max}$ | $\Theta_S$ | $R_{\mathrm{sw},\max}$ | $\Theta_{\mathrm{sw}}$ | $R_{\mathrm{ej},\max}$ | $\Theta_{\mathrm{ej}}$ | $R_{\mathrm{AM},\max}$ | $\Theta_{\mathrm{AM}}$ |
|---|---|---|---|---|---|---|---|---|
| NA-MEMD | 0.58 | 15.88° | 0.50 | 24.19° | 0.44 | 28.78° | 0.65 | 71.69° |
| uniEMD | 0.27 | 27.86° | 0.35 | 9.64° | 0.40 | 11.78° | 0.64 | 64.12° |

the NA-MEMD. The superposition is maximally affected and the averaged correlation coefficient is approximately divided in half. Hence, the improper scale alignment inhibits a precise determination of the actual strength of inner-outer interaction. In addition, the high frequency variation of the quantities in the temporal domain is significantly increased using the univariate EMD as indicated by the grey distribution exemplarily shown for the superposition. Thus, the univariate EMD is less suited for providing an accurate temporal coherence between the large scales of subsequent time steps as it was already discussed in Appendix A 4. These effects certainly influence the associated inclination angles. As shown by comparing Fig. 22(b) with Fig. 9(a) and inspecting the averaged angles in Table VI, the superposition is characterized by increased angles using the univariate EMD, while the other phenomena feature lower values. For all phenomena, the time-dependent fluctuations are massively increased compared to the NA-MEMD findings.

In summary, the interaction analysis at $\{y^+_{\mathrm{NW1}} = 1, y^+_{\mathrm{OL}} = 123\}$ based on a univariate scale separation yields reduced maximum correlation coefficients, altered inclination angles, and higher time-dependent variations of both quantities compared to the simultaneous scale separation of all involved fluctuations by the NA-MEMD. These findings corroborate the necessity of a multivariate approach to accurately determine the strength and the angle of the inner-outer interaction in a spatiotemporal analysis.

## APPENDIX C: AMPLITUDE CALCULATION VIA THE 2D ANALYTIC SIGNAL

To study the amplitude modulation within 2D large-scale velocity fields, the respective 2D amplitudes have to be determined. They are obtained from the 2D analytic signal introduced by Wietzke *et al.* [32] and the reader is referred to this publication for detailed information. The approach is conducted localized using a convolution mask of size $(2m + 1{\times}2m + 1)$, i.e., the amplitude value of a single pixel $(i, j)$ is calculated based on its neighborhood with $m$ adjacent pixels in both directions (here, $m = 3$). In the following, the procedure is outlined for the extract around an exemplary pixel, which is shown in Fig. 23 with the applied notation.

For the analysis of amplitude modulation, the amplitudes of the streamwise large-scale components $u'_{\mathrm{OL,LS2}}, u'_{\mathrm{NW,LS2}}$ are calculated but for conciseness, the respective component is just referred to as $u$ in the following. The extract of the velocity data, i.e., the pixel $(i, j)$ and its neighborhood, is defined by

$$u_w = u(i - m : i + m, j - m : j + m). \tag{C1}$$

For simplicity, a new coordinate system $(ii, jj)$ is introduced. As shown in Fig. 23, its origin coincides with $(i, j)$ and it spans $(ii, jj) = (-m : m, -m : m)$. When referring to the 2D matrix containing the grid data, the notation $(II, JJ)$ will be used.

The velocity extract $u_w(ii, jj)$ is multiplied by the first order generalized 2D Hilbert convolution kernel

$$u_{c1}(ii, jj) = u_w(ii, jj)c_1(ii, jj), \tag{C2}$$

with

$$c_1(ii, jj) = \frac{1}{2\pi(s^2 + ii^2 + jj^2)^{3/2}} \tag{C3}$$

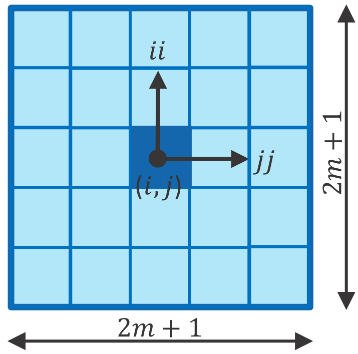


FIG. 23. Schematic illustration of the pixel $(i, j)$ and its neighborhood with the notation used for outlining the amplitude calculation.

and by the second order generalized 2D Hilbert convolution kernel,

$$u_{c2}(ii, jj) = u_w(ii, jj)c_2(ii, jj), \tag{C4}$$

with

$$c_2(ii, jj) = -\frac{s[2s^2 + 3(ii^2 + jj^2)] - 2(s^2 + ii^2 + jj^2)^{3/2}}{2\pi(ii^2 + jj^2)^2(s^2 + ii^2 + jj^2)^{3/2}}. \tag{C5}$$

The scale space parameter $s$ acts as a low pass filter on $u_w$ and essentially defines the strength of amplitude. However, in the current application, its influence will be eliminated in a final step in which the velocity amplitudes are scaled according to the original velocity values [see Eq. (C14)].

Next, the first- and second-order Hilbert transformed components are determined:

$$u_{ws} = \sum_{ii=-m}^{ii=m}\sum_{jj=-m}^{jj=m} u_w(ii, jj), \tag{C6}$$

$$u_i = \sum_{ii=-m}^{ii=m}\sum_{jj=-m}^{jj=m} II(ii, jj)u_{c1}(ii, jj), \tag{C7}$$

$$u_j = \sum_{ii=-m}^{ii=m}\sum_{jj=-m}^{jj=m} JJ(ii, jj)u_{c1}(ii, jj), \tag{C8}$$

$$u_{ii} = \sum_{ii=-m}^{ii=m}\sum_{jj=-m}^{jj=m} II^2(ii, jj)u_{c2}(ii, jj), \tag{C9}$$

$$u_{ij} = \sum_{ii=-m}^{ii=m}\sum_{jj=-m}^{jj=m} II(ii, jj)JJ(ii, jj)u_{c2}(ii, jj), \tag{C10}$$

$$u_{jj} = \sum_{ii=-m}^{ii=m}\sum_{jj=-m}^{jj=m} JJ^2(ii, jj)u_{c2}(ii, jj). \tag{C11}$$

Based on these components, an interim amplitude $\hat{u}_{\rm int}$ at the pixel $(i, j)$ is obtained via

$$\hat{u}_{\rm int} = \frac{1}{2}\sqrt{u_{ws}^2 + \frac{u_i^2 + u_j^2}{1+b}}, \tag{C12}$$

with

$$b = \frac{\sqrt{\left[\frac{1}{2}(u_{ii} - u_{jj})\right]^2 + u_{ij}^2}}{|\frac{1}{2}u_{ws}|}. \tag{C13}$$

The procedure is repeated for all pixels of the respective large-scale velocity component to obtain the complete 2D interim amplitude distribution. Finally, it is rescaled to its correct magnitude using

$$\hat{u} = \hat{u}_{\rm int}\frac{|u|_{\rm max}}{\hat{u}_{\rm int,max}}. \tag{C14}$$

Note that all quantities in Eq. (C14) are matrices that represent the respective 2D field components. Thus, the maximum values of $|u|$ and $\hat{u}_{\rm int}$ are determined over the whole 2D domain.

---


[1] H.-Y. Liu, T.-L. Bo, and Y.-R. Liang, The variation of large-scale structure inclination angles in high Reynolds number atmospheric surface layers, Phys. Fluids **29**, 035104 (2017).

[2] L. Agostini and M. A. Leschziner, On the influence of outer large-scale structures on near-wall turbulence in channel flow, Phys. Fluids **26**, 075107 (2014).

[3] R. Mathis, N. Hutchins, and I. Marusic, Large-scale amplitude modulation of the small-scale structures in turbulent boundary layers, J. Fluid Mech. **628**, 311 (2009).

[4] M. Bernardini and S. Pirozzoli, Inner/outer layer interactions in turbulent boundary layers: A refined measure for the large-scale amplitude modulation mechanism, Phys. Fluids **23**, 061701 (2011).

[5] W. Baars, K. M. Talluru, N. Hutchins, and I. Marusic, Wavelet analysis of wall turbulence to study large-scale modulation of small scales, Exp. Fluids **56**, 188 (2015).

[6] E. Mäteling, M. Klaas, and W. Schröder, Detection of small-scale/large-scale interactions in turbulent wall-bounded flows, Phys. Rev. Fluids **5**, 114610 (2020).

[7] B. Ganapathisubramani, N. Hutchins, J. P. Monty, D. Chung, and I. Marusic, Amplitude and frequency modulation in wall turbulence, J. Fluid Mech. **712**, 61 (2012).

[8] G. Pathikonda and K. T. Christensen, Investigation of inner-outer interactions in a turbulent boundary layer using high-speed particle image velocimetry, Phys. Rev. Fluids **4**, 034607 (2019).

[9] J. Jiménez, Cascades in wall-bounded turbulence, Annu. Rev. Fluid Mech. **44**, 27 (2012).

[10] I. Marusic, W. J. Baars, and N. Hutchins, Scaling of the streamwise turbulence intensity in the context of inner-outer interactions in wall turbulence, Phys. Rev. Fluids **2**, 100502 (2017).

[11] G. I. Taylor, The spectrum of turbulence, Proc. R. Soc. London A **164**, 476 (1938).

[12] D. J. Dennis and T. B. Nickels, On the limitations of Taylor's hypothesis in constructing long structures in a turbulent boundary layer, J. Fluid Mech. **614**, 197 (2008).

[13] C. Atkinson, N. A. Buchmann, and J. Soria, An experimental investigation of turbulent convection velocities in a turbulent boundary layer, Flow, Turbul. Combust. **94**, 79 (2015).

[14] J. Graham, K. Kanov, X. Yang, M. Lee, N. Malaya, C. C. Lalescu, R. Burns, G. Eyink, A. Szalay, R. D. Moser *et al.*, A web services accessible database of turbulent channel flow and its use for testing a new integral wall model for LES, J. Turbul. **17**, 181 (2016).

[15] N. E. Huang, Z. Shen, S. R. Long, M. C. Wu, H. H. Shih, Q. Zheng, N.-C. Yen, C. C. Tung, and H. H. Liu, The empirical mode decomposition and the Hilbert spectrum for nonlinear and nonstationary time series analysis, Proc. R. Soc. London A **454**, 903 (1998).

[16] E. Mäteling, M. Klaas, and W. Schröder, Simultaneous stereo PIV and MPS3 wall-shear stress measurements in turbulent channel flow, Optics **1**, 40 (2020).

[17] N. Rehman and D. P. Mandic, Multivariate empirical mode decomposition, Proc. R. Soc. A **466**, 1291 (2010).

[18] Y. Xia, B. Zhang, W. Pei, and D. P. Mandic, Bidimensional multivariate empirical mode decomposition with applications in multiscale image fusion, IEEE Access **7**, 114261 (2019).

[19] E. Perlman, R. Burns, Y. Li, and C. Meneveau, Data exploration of turbulence simulations using a database cluster, in *Proceedings of the ACM/IEEE Conference on Supercomputing* (ACM Press, New York, NY, 2007), pp. 1–11.

[20] Y. Li, E. Perlman, M. Wan, Y. Yang, C. Meneveau, R. Burns, S. Chen, A. Szalay, and G. Eyink, A public turbulence database cluster and applications to study lagrangian evolution of velocity increments in turbulence, J. Turbul. **9**, N31 (2008).

[21] I. Marusic, R. Mathis, and N. Hutchins, High Reynolds number effects in wall turbulence, Int. J. Heat Fluid Flow **31**, 418 (2010).

[22] J. C. Nunes, O. Niang, Y. Bouaoune, E. Delechelle, and P. Bunel, Texture analysis based on the bidimensional empirical mode decomposition with gray-level co-occurrence models, in *Proceedings of the 7th International Symposium on Signal Processing and Its Applications* (IEEE, Piscataway, NJ, 2003), Vol. 2, pp. 633–635.

[23] N. Rehman and D. P. Mandic, Filter bank property of multivariate empirical mode decomposition, IEEE Trans. Signal Process. **59**, 2421 (2011).

[24] N. Rehman, C. Park, N. E. Huang, and D. P. Mandic, EMD via MEMD: Multivariate noise-aided computation of standard EMD, Adv. Adapt. Data Anal. **5**, 1350007 (2013).

[25] Z. Wu and N. E. Huang, A study of the characteristics of white noise using the empirical mode decomposition method, Proc. R. Soc. London A **460**, 1597 (2004).

[26] P. Flandrin, G. Rilling, and P. Goncalves, Empirical mode decomposition as a filter bank, IEEE Signal Process. Lett. **11**, 112 (2004).

[27] Z. Liu, R. J. Adrian, and T. J. Hanratty, Large-scale modes of turbulent channel flow: Transport and structure, J. Fluid Mech. **448**, 53 (2001).

[28] J. C. Del Alamo, J. Jiménez, P. Zandonade, and R. D Moser, Scaling of the energy spectra of turbulent channels, J. Fluid Mech. **500**, 135 (2004).

[29] J. P. Monty, J. Stewart, R. Williams, and M. Chong, Large-scale features in turbulent pipe and channel flows, J. Fluid Mech. **589**, 147 (2007).

[30] E. Mäteling, M. Klaas, and W. Schröder, Study on large-scale amplitude modulation of near-wall small-scale structures in turbulent wall-bounded flows, in *Proceedings of the 22nd STAB/DGLR Symposium on New Results in Numerical and Experimental Fluid Mechanics* (Springer Nature, Berlin, 2021).

[31] I. Marusic, R. Mathis, and N. Hutchins, Predictive model for wall-bounded turbulent flow, Science **329**, 193 (2010).

[32] L. Wietzke, G. Sommer, and O. Fleischmann, The geometry of 2D image signals, in *Proceedings of the IEEE Conference on Computer Vision and Pattern Recognition* (IEEE, Piscataway, NJ, 2009), pp. 1690–1697.

[33] M. Felsberg and G. Sommer, The monogenic signal, IEEE Trans. Signal Process. **49**, 3136 (2001).

[34] See Supplemental Material at http://link.aps.org/supplemental/10.1103/PhysRevFluids.7.034603 for the temporal evolution of the intrinsic mode functions obtained by the 2D NA-MEMD for the data at $\{y^+_{\mathrm{NW1}} = 1, y^+_{\mathrm{OL}} = 123\}$.

[35] B. J. Balakumar and R. J. Adrian, Large-and very-large-scale motions in channel and boundary-layer flows, Philos. Trans. R. Soc. A **365**, 665 (2007).

[36] L. H. Hellström, B. Ganapathisubramani, and A. J. Smits, The evolution of large-scale motions in turbulent pipe flow, J. Fluid Mech. **779**, 701 (2015).

[37] Y. Huang, F. G. Schmitt, Z. Lu, and Y. Liu, An amplitude-frequency study of turbulent scaling intermittency using empirical mode decomposition and hilbert spectral analysis, Europhys. Lett. **84**, 40010 (2008).

[38] C. Cheng, W. Li, A. Lozano-Durán, and H. Liu, Identity of attached eddies in turbulent channel flows with bidimensional empirical mode decomposition, J. Fluid Mech. **870**, 1037 (2019).

[39] R. Mathis, I. Marusic, N. Hutchins, and K. Sreenivasan, The relationship between the velocity skewness and the amplitude modulation of the small scale by the large scale in turbulent boundary layers, Phys. Fluids **23**, 121702 (2011).
[40] L. Agostini, M. Leschziner, and D. Gaitonde, Skewness-induced asymmetric modulation of small-scale turbulence by large-scale structures, Phys. Fluids **28**, 015110 (2016).
[41] See Supplemental Material at http://link.aps.org/supplemental/10.1103/PhysRevFluids.7.034603 for the temporal evolution of the near-wall and the outer-layer large scales obtained by the 2D NA-MEMD for the data at $\{y^+_{\mathrm{NW5}} = 5, y^+_{OL} = 123\}$.
[42] M. Abbassi, W. J. Baars, N. Hutchins, and I. Marusic, Skin-friction drag reduction in a high-Reynolds-number turbulent boundary layer via real-time control of large-scale structures, Int. J. Heat Fluid Flow **67**, 30 (2017).
[43] I. Marusic and W. D. C. Heuer, Reynolds Number Invariance of the Structure Inclination Angle in Wall Turbulence, Phys. Rev. Lett. **99**, 114504 (2007).
[44] R. Mathis, N. Hutchins, and I. Marusic, A predictive inner–outer model for streamwise turbulence statistics in wall-bounded flows, J. Fluid Mech. **681**, 537 (2011).
[45] https://git.rwth-aachen.de/aia/bimemd
[46] https://doi.org/10.7281/T10K26QW
[47] Z. Wu and N. E. Huang, Ensemble empirical mode decomposition: A noise-assisted data analysis method, Adv. Adapt. Data Anal. **1**, 1 (2009).
[48] N. E. Huang, M.-L. C. Wu, S. R. Long, S. S. Shen, W. Qu, P. Gloersen, and K. L. Fan, A confidence limit for the empirical mode decomposition and Hilbert spectral analysis, Proc. R. Soc. London A **459**, 2317 (2003).
[49] P. Singh, S. D. Joshi, R. K. Patney, and K. Saha, The Hilbert spectrum and the energy preserving empirical mode decomposition, arXiv:1504.04104.
[50] See Supplemental Material at http://link.aps.org/supplemental/10.1103/PhysRevFluids.7.034603 for the temporal evolution of the near-wall and the outer-layer large scales obtained by the univariate EMD, the MEMD, and the NA-MEMD for the data at $\{y^+_{\mathrm{NW1}} = 1, y^+_{\mathrm{OL}} = 123\}$.